Published in final edited form as:
J Comput Phys. 2013 July 1; 244: 41–62. doi:10.1016/j.jcp.2012.08.036.

Fluid-structure interaction of an aortic heart valve prosthesis driven by an animated anatomic left ventricle

Trung Bao Le and **Fotis Sotiropoulos**
Saint Anthony Falls Laboratory, Department of Civil Engineering, University of Minnesota, 2 Third Ave SE, Minneapolis, MN 55414

Abstract

We develop a novel large-scale kinematic model for animating the left ventricle (LV) wall and use this model to drive the fluid-structure interaction (FSI) between the ensuing blood flow and a mechanical heart valve prosthesis implanted in the aortic position of an anatomic LV/aorta configuration. The kinematic model is of lumped type and employs a cell-based, FitzHugh-Nagumo framework to simulate the motion of the LV wall in response to an excitation wavefront propagating along the heart wall. The emerging large-scale LV wall motion exhibits complex contractile mechanisms that include contraction (twist) and expansion (untwist). The kinematic model is shown to yield global LV motion parameters that are well within the physiologic range throughout the cardiac cycle. The FSI between the leaflets of the mechanical heart valve and the blood flow driven by the dynamic LV wall motion and mitral inflow is simulated using the curvilinear immersed boundary (CURVIB) method [1, 2] implemented in conjunction with a domain decomposition approach. The computed results show that the simulated flow patterns are in good qualitative agreement with *in vivo* observations. The simulations also reveal complex kinematics of the valve leaflets, thus, underscoring the need for patient-specific simulations of heart valve prosthesis and other cardiac devices.

Keywords

cardiac electrophysiology; FitzHugh-Nagumo model; left heart hemodynamics; patient-specific modeling; bi-leaflet mechanical heart valve; fluid structure interaction

1. Introduction

In spite of significant recent advances in imaging modalities for studying cardiac hemodynamics [3, 4, 5], present-day *in vivo* measurement techniques can only resolve large scale blood flow features [6]. Understanding flow patterns in the heart at physiologic conditions and scales sufficiently fine for establishing quantitatively links between heart disease and patient-specific hemodynamics continues to remain a major research challenge. This challenge becomes even more formidable when prosthetic heart valves are implanted [7]. For instance, *in vitro* experiments with simplified models of the left heart [8, 9, 10, 11] and fluid-structure interaction (FSI) computational studies in straight [12, 13, 14, 15, 1, 2, 16, 17] and anatomic [18] aorta geometries have clearly shown that at physiologic conditions the presence of a prosthetic heart valve gives rise to complex flow patterns

characterized by fine scale flow structures and transition to turbulence. This complex and dynamically rich flow environment is widely believed to be the major culprit for the clinical complications that arise following implantation of valve prosthesis [19, 20]. Considering the resolution limitations of present-day *in vivo* measurement techniques and the complexity of the underlying flow environment, high-resolution numerical simulation appears to be the only viable option for advancing our understanding of cardiac hemodynamics especially in the presence of prosthetic heart valves. For computational algorithms, however, to yield clinically relevant results their degree of realism needs to be drastically enhanced by incorporating into the modeling framework multi-physics elements of cardiac function along with input from modern imaging modalities and *in vivo* measurement techniques. In this paper, we report some progresses in that direction by developing a high-resolution FSI algorithm for simulating a bi-leaflet mechanical heart valve (BMHV) implanted in the aortic position of an anatomic beating left ventricle (LV) whose wall motion is simulated via a lumped-parameter model inspired by cardiac electro-physiology.

Critical prerequisite for simulating the motion of a BMHV in a beating left heart is the development of a model for simulating the LV hemodynamics, which is dominated by the complex interaction of the blood flow with the compliant and continuously deforming heart walls. Patient-specific simulation of the ensuing FSI problem from first principles is a formidable task since total heart function emerges as the result of the coupled interaction of the blood flow with a host of molecular, electrical and mechanical processes that occur across a wide range of scales [21, 22]. At the cellular level contractile forces that cause the heart muscle to move are generated as cells are repolarized or depolarized by absorption or release of several ions (such as $[Ca^{+}]$, $[Cl]^{-}$, $[Na]^{+}$, $[K]^{+}$ etc., respectively). The resulting electrical excitation wave propagates throughout the heart via a fast conducting system known as the Purkinje fibres network [23]. Such cable-like conducting system controls the myocardial activation sequence and is thus very important for the emerging LV contraction [24]. At the tissue level, the heart wall is structured into three main layers: the outermost epicardium; the myocardium; and the innermost endocardium, which is in contact with the blood flow. The myocardium is significantly thicker than two other layers and contributes most of the contractile forces. The myocardial muscle fibers bind themselves into “sheet-like” structures [25, 21], which are laid on top of each other wrapping around the LV chamber from the base to the apex and vice versa. At the organ level, the activation of cardiac cells also depends on the ions transport through the system of coronary arteries. Therefore, simulation of the whole heart organ continues to remain elusive as it would require a multi-physics simulation framework spanning a variety of scales ranging from metabolism of cardiac cells to the large scale fate transport (oxygen, ions .etc) in coronary arteries and the aorta [26, 4, 22].

Available models for simulating blood flow in the heart can be broadly classified based on their spatial dimension and degree of sophistication into four categories [27, 28]: 1) Lumped and one-dimensional (1D) model; 2) Two-dimensional (2D) models; 3)Three-dimensional (3D) models with prescribed heart wall motion; and 4) Three-dimensional models with coupled FSI simulation of blood flow and tissue mechanics (3D-FSI).

1D models rely on a non-linear relation between the LV pressure and the blood flow via an empirical, black box simulator [29, 30, 31, 32, 27, 33]. Such models are simple to use and can efficiently obtain the pressure and volume curve but they are inherently incapable of providing the flow field inside the LV chamber.

2D models typically simulate idealized LV models [34, 35, 36]. Although these models can incorporate more physics than their 1D counter-part, their extension to simulate realistic LV flow in patient-specific geometries is difficult, if not impossible.

3D models employ a three-dimensional LV geometry, which can be idealized [37] or anatomic [38], with the wall motion prescribed either through simple analytical functions [37] or using patient-specific data [39, 40, 38]. In the latter category of 3D models [39, 40, 38], the patient-specific LV kinematics is reconstructed directly from *in vivo* MRI measurements. Such models can incorporate a high-degree of patient-specific realism provided that imaging modalities of sufficient resolution are available to accurately reconstruct the wall motion. Since the present day scanning frequency per heart beat (frames/s) is technologically limited, however, temporal interpolation between successive MRI images must be used to reconstruct the LV wall motion over the cardiac cycle [41, 39, 40, 38]. Obviously the accuracy of the resulting kinematics, and consequently the clinical relevance of the 3D hemodynamic model, depends both on the accuracy of the interpolation technique and the initial temporal resolution of the MRI images. The spatial resolution of MRI can also be a potential source of error and uncertainty especially when subtle modes of the LV wall motion, such as twisting due to spiral fiber contraction [28], are to be incorporated in the model. The reconstruction of such feature ensures the fine scale structure of the flow be capture realistically.

From the modeling sophistication standpoint 3D-FSI models [42, 43, 44, 45, 46, 47, 28, 48], are the most advanced as the heart wall is allowed to interact with the blood flow in a fully coupled manner. Critical prerequisite for the success of such models is the development of patient-specific constitutive models for the cardiac tissue that not only account or the interaction of blood flow with the heart wall but also for the interaction of the heart with surrounding organs [22]. These complexities require extensive assumptions on the heart wall structure and electrical activation [28] to enable fully-coupled blood-tissue interaction simulations, which could compromise the physiologic realism of the resulting models [45, 44, 46, 28]. The first attempt to develop such a model was the pioneering work by Peskin and co-workers [49, 50] who assumed that myocardial fibers are discretely distributed. In this model the heart was assumed to be embedded in a periodic domain filled with fluid and the simulations were carried out at conditions that were not physiologic [50]. More recent versions of this model have been able to carry out simulations at higher cardiac volume flow rate [51, 52, 43, 17]. Other 3D-FSI models have attempted to raise the degree of patient-specific modeling realism by incorporating information acquired from non-invasive imaging modalities. Such models have incorporated continuous fiber distribution into the wall model [28] and even attempted to couple the electrical excitation with the tissue response [47, 22]. The main challenges confronting this class of models stem from the previously discussed limitations in the resolution of imaging modalities as well as the extensive simplifying assumptions that need to be incorporated in the FSI model.

With only exception the work by Peskin and co-workers [51, 52], who simulated native heart valves, all previously discussed computational models have focused on the LV hemodynamics and neglected the presence of heart valves. Furthermore, and to the best of our knowledge, FSI simulations of heart valve prosthesis ([see 53, for a recent review]) have been thus far carried out in idealized straight aorta models [54, 55, 15, 2, 16, 17] or anatomic aorta models [56]. For both cases the valve motion and so-induced systolic phase hemodynamics were driven by an imposed flow wave form at the inlet of the computational domain. To our knowledge, high resolution FSI simulation of an implanted heart valve prosthesis in a patient-specific beating left heart under physiologic conditions has yet to be reported in the literature.

In this work, we report computational advances that have enabled us to carry out high-resolution simulations of patient-specific LV hemodynamics with a BMHV (see Fig. 1) implanted in the aortic position. We develop a lumped-parameter, cell-based model of the LV wall motion, which is inspired by cardiac electro-physiology and yields physiologic LV

kinematics during the entire cardiac cycle. We use this model to prescribe the motion of the anatomic LV system in our simulation. The so prescribed LV wall motion drives the hemodynamics in the LV/aorta domain and the ensuing motion of the implanted BMHV leaflets, which is calculated via a coupled FSI approach.

In what follows, we begin by presenting the cell-based model of the LV wall kinematics. Subsequently we present the FSI method for simulating flows in arbitrarily complex domains with moving immersed boundaries. The method is based on the Curvilinear Immersed Boundary (CURVIB) method developed by [1] and extended to FSI problems by [2]. Finally we demonstrate the potential of the computational framework by applying it to simulate the flow in a domain consisting of an anatomic LV and the aorta, reconstructed from MRI data from a healthy volunteer, with the BMHV implanted in the aortic position and a flow wave form imposed at the mitral orifice to simulate the effect of the mitral valve. Comparisons with available data are presented to demonstrate that the method yields physiologic results and future extension and generalization of the method are discussed.

2. Computational Methods

We simulate incompressible flow of a Netwonian fluid in the computational domain shown in Fig. 2. The domain consists of two sub-domains: the LV and the aorta sub-domains, respectively. The LV sub-domain contains the left ventricular chamber with incoming flow from the mitral orifice. This sub-domain is filled with fluid whose motion is driven by the moving heart wall. The LV sub-domain is connected to the aorta sub-domain via the LV outflow track (LVOT) interface. The aorta sub-domain contains the BMHV (solid domain) embedded within the fluid-filled aorta (fluid domain).

We denote the fluid domain as Ω_f and the solid domain as Ω_s (see Fig. 2b). The subscripts f and s will be used to indicate the fluid and solid domains, respectively, throughout this manuscript. The interface between the fluid and the solid domain is denoted as $\Gamma = \partial\Omega_F = \partial\Omega_S$. The portions of the interface between the BMHV leaflet interface and the blood flow is denoted as Γ_{FSI}, since the motion of the leaflets is determined via a coupled FSI algorithm in our model. The endocardium surface, the mitral inlet, the aorta and the outlet of the descending aorta are denoted as Γ_{LV}, Γ_{inlet}, Γ_{aorta} and Γ_{outlet}, respectively. Therefore, in our computational domain the interface Γ between solid and fluid is given by $\Gamma = \Gamma_{FSI} \cup \Gamma_{LV} \cup \Gamma_{inlet} \cup \Gamma_{aorta} \cup \Gamma_{outlet}$ as shown in Fig. 2.

In our model we neglect the motion of the aortic domain, Γ_{aorta} and Γ_{outlet}, as well the motion of the portion of the LV domain which is close to the mitral opening Γ_{inlet}. All other parts of the boundary move either with prescribed motion or as the result of coupled non-linear FSI. We can thus express Γ as follows: $\Gamma = \Gamma_M \cup \Gamma_S$, where Γ_M is the moving portion of the boundary ($= \Gamma_{FSI} \cup \Gamma_{LV}$) and Γ_S is the portion of the boundary that is held stationary ($= \Gamma_{inlet} \cup \Gamma_{aorta} \cup \Gamma_{outlet}$).

We discretize the interface between the moving portion of the boundary and the fluid domain using a set of material points [57] $i = 1, I$ with coordinates $\mathbf{x_i}$ defining the interface $\Gamma_M = \Gamma_M(\mathbf{x_i})$. The motion of material points are tracked in a Lagrangian manner by solving the following equation:

$$\mathbf{v}_i = \frac{d\mathbf{x}_i}{dt} \quad \forall \mathbf{x}_i \in \Gamma_M \qquad (1)$$

where $\mathbf{v}_i$ is the velocity vector of the i^{th} material point. Since the two portions, Γ_{FSI} and Γ_{LV}, of Γ_M move as a result of different physical processes, we treat each one of them with different numerical techniques described below.

2.1. The left ventricle kinematics model for Γ_{LV}

In this work, we develop a novel model for reconstructing physiologic LV kinematics by adopting a lumped-parameterization approach [29, 30, 27], which is simple and computationally efficient yet sufficiently sophisticated to reproduce the essential physiologic features of the LV kinematics including features that are difficult to obtain from MRI data such as the LV wall spiral twisting and untwisting motions.

The model to be described below is applied to animate an anatomical left heart geometry reconstructed from MRI scanned images of a healthy subject provided to us by the Cardiovascular Fluid Mechanics Laboratory of the Georgia Institute of Technology. The ventricle model is shown in Fig. 3 and its basic dimensions are as follows: the long and short LV axes length are $L = 80mm$ and $D_L = 47mm$, respectively; the diameter of the aorta at the $LVOT$ is $D = 26.7\ mm$; and the mitral annulus diameter is $D_M = 37mm$. Due to the BMHV implantation the mitral annulus is blocked partially. The mitral orifice opening area is reduced to a circular area with diameter $D_{orifice} = 22.5\ mm$ and the effective mitral opening area is $MVA = 3.97\ cm^2$, which lies entirely in the physiological range [58, 59] of an adult subject. No mitral valve is included in the model and thus the mitral orifice is set to be fully open during diastole and fully closed during systole.

We seek to develop a model that enables us to estimate and prescribe the activation sequence, expressed in terms of a time-dependent transmembrane potential $p(t)$. It is important to emphasize, however, that $p(t)$ in our model should be viewed as a parameter of a lumped model, which is calibrated to animate the LV wall motion. With $p(t)$ given, a lumped model for the electrical excitation of the endocardium is derived as a function of $p(t)$ [60] based on a heuristic approach [30]. The so obtained electrical excitation drives through the proposed model muscle deformation and animates the LV wall. Such excitation sequence depends on several factors, including the transport of ions in the coronary arteries as well as the transmission of the electrical current in the Purkinje network. Therefore, incorporating in the model a specific $p(t)$ functionally corresponds to a lumped-modeling approach that reflects the emergent large scale dynamics of the heart wall. Nevertheless, the development of our model is guided by cell-based processes and, as we will show, it can be calibrated to yield physiologic characteristics of the wall motion.

The model is based on the following three assumptions. First, we assume that the base and the apex of the LV are stationary. Second, we model the endocardium as the wall surface since this is the only layer of the heart muscle that comes in contact with the blood flow. The endocardium surface Γ_{LV} is discretized with an unstructured grid with J_e material nodes as shown in Fig. 4. Each material node j ($j = 1, J_e$) is assumed to represent one endocardium cell. Third, the motion of each material node in response to the cardiac electrical stimulation is assumed to be a function of a time-dependent transmembrane potential $p(t)$.

The instantaneous velocity vector of the j^{th} material node ($j \in \Gamma_{LV}$) can be expressed as follows:

$$\mathbf{v_j}(t) = \frac{d\mathbf{x_j}}{dt} = v_j^r(t)\mathbf{i}_r + v_j^\theta(t)\mathbf{i}_\theta + v_j^z(t)\mathbf{i}_z \quad (2)$$

where v_j^r, v_j^θ, and v_j^z are the radial, tangential and axial velocity components, respectively, and $\mathbf{i_r}$, $\mathbf{i_\theta}$, and $\mathbf{i_z}$ are the corresponding unit vectors (see Fig. 3 for coordinate definition). Starting from a known instantaneous configuration of the LV wall, i.e. all position vectors $\mathbf{x_j}$ for $j \in \Gamma_{LV}$ are known at the initial time t_0, and assuming that the velocity vector of each cell is known as a function of time, Eq. 2 can be readily integrated in time for all material points $j = 1, J_e$ to update the shape of the LV wall at the next instant in time. In what follows, we

develop a model for the time dependent velocity vector of each material node that ultimately relates the wall velocity to the time-dependent transmembrane potential $p(t)$.

To develop a mathematical model that couples electrical (p) and mechanical ($\mathbf{v}_j$) activity of the heart, we begin by considering existing electro-mechanical models (see [61], for a recent review). Following [61], the cardiac tissue mechanical stress can be decomposed as the sum of a passive and active component. The passive stress component is the classical second Piola-Kirchoff tensor while the active stress T_a expresses the stress that develops in the cardiac tissue during cellular depolarization. In the model proposed by Nash and Panfilov [61], T_a is expressed as the function of the non-dimensional transmembrane potential p via the following equation:

$$\begin{aligned} \frac{\partial T_a}{\partial t} + \eta(p) T_a &= \eta(p) K_{T_a} p \\ \eta(p) &= \begin{cases} \eta_0 & \text{for } p < 0.05 \\ 10\eta_0 & \text{for } p \geq 0.05 \end{cases} \end{aligned} \quad (3)$$

where K_{T_a} is a coefficient that controls the amplitude of the active stress response. Equation 3 shows that the temporal variation of the active stress is governed by a wave propagation in the medium excited by the transmembrane potential. Since the instantaneous velocity of each material point is a function of both the passive and active stress components, and inspired by the underlying wave-like electromechanical physical processes implied by Eq. 3, we propose a simple model that expresses the instantaneous velocity magnitude $v_j = |\mathbf{v_j}(t)|$ of each material point as a function of a time-dependent, wave propagation component (G) (due to the active stress) and a spatial component S (due to the passive stress) as follows:

$$v_j(t) = G(\mathbf{x_j}, t) \mathrm{S}(\mathbf{x_j}) \quad (4)$$

The spatial distribution part of the stress is modeled as a power law [62] expressed in the cylindrical coordinate system shown in Fig. 3. More specifically, we assume that S varies along the endocardium as a function of the radial (r_j) and longitudinal (z_j) coordinates of each material point as follows:

$$\mathrm{S}(\mathbf{x_j}) = \mathrm{S}(r_j, z_j) = \left(\frac{2r_j}{D_L}\right)^2 \left(\frac{z_j}{L}\right)^{1.5} \quad (5)$$

The wave propagation component G in Eq. 4 can be thought of as the total transmembrane current for each cardiac cell, which depends on $p(t)$. To develop a model for G we assume that its spatial and temporal variation is governed by FitzHugh-Nagumo type models, which have previously been used succesfully for modeling cardiac tissues [61, 63, 64]. In its simplest form the FitzHugh-Nagumo model reads as follows [65, 66, 64, 61]:

$$\begin{aligned} G &= \nabla \cdot (\mathrm{D} \nabla p) \\ \frac{\partial p}{\partial t} &= \nabla \cdot (\mathrm{D} \nabla p) - c_1 p(p - c_0)(p - 1) - q \\ \frac{\partial q}{\partial t} &= b(p - dq) \end{aligned} \quad (6)$$

where D is the media conductivity tensor, the parameters c_1 and c_0 are model-dependent constants, q is the recovery variable, and b, d are recovery constants. To simulate the excitation of the whole media, one needs to solve the system of Eqs. 6 to get the spatial distribution of the current G [61]. Since for a patient-specific case, the conductivity D is not known in advance Eqs. 6 cannot be solved.

To circumvent this difficulty, we employ a lumped modeling approach by assuming that the patient-specific transmembrane potential $p(t)$ is somehow known, say it can be measured *in vivo* via a modality like electrocardiography or it can be obtained via patient-specific calibration. By adopting this assumption we eliminate the need for solving the FitzHugh-Nagumo system of equations for each material node. However, the challenge of deriving a reasonable approximation for G as a function of p still remains.

We note that the electrical excitation of a given cardiac cell, which is expressed in terms of G, depends on processes that occur within the cell itself as well as the interconnections of the cell with neighboring cells via the Purkinje network [21]. Therefore, we propose to model $G(\mathbf{x_j}, t)$ as a product of a local, time-dependent part $E_j(t)$, which is a lumped model of processes in the given cardiac cell, and a wave-propagation part $S(\mathbf{x_j}, t)$, which accounts for interconnections between neighboring cardiac cells, as follows:

$$G(\mathbf{x_j}, t) = E_j(t) S(\mathbf{x_j}, t) \quad (7)$$

In the Eq. 7, E_j is assumed to be a function of the time-dependent potential p_j, i.e. $E_j(t) = E[p_j(t)]$. We assume that E has similar form with that of the current G under equilibrium condition, denoted as G_e. Following [61], we can obtain the equilibrium solution from the FitzHugh-Nagumo system of equations by setting $\frac{\partial p}{\partial t}=0$ and $\frac{\partial q}{\partial t}=0$ in Eqs. 6. Doing so, we obtain for an isolated cell at equilibrium the following expression for G_e:

$$\begin{aligned} G_e &= c_1\, p(p - c_0)(p - 1) + q \\ q &= \tfrac{p}{d} \end{aligned} \quad (8)$$

Or:

$$G_e = c_1\, p(p - c_0)(p - 1) + c_2\, p \quad (9)$$

To account for transient effects in $p(t)$ and $q(t)$, we express E_j as a function of G_e but also introduce exponential decay terms as follows:

$$E_j(t) = c_1\, p_j(t)[p_j(t) - c_0][p_j(t) - 1] + c_2[p_j(t) - 1][1 - \exp(-c_3\, p_j(t))] \quad (10)$$

where the functional $p_j(t)$ and the model constants c_0, c_1, c_2 and c_3 are selected as part of the calibration of the model in the range reported in previous studies [66] (see below).

The $S(\mathbf{x_j}, t)$ term, which models the large scale interconnection between cells, has been observed *in – vivo* to be well described as a large scale mechanical wave [67, 68, 69]. We thus propose to model S in Eq. 7 as a sine wave function [70, 68] with scaling frequency factor f_s and phase lag φ, as follows:

$$S(\mathbf{x_j}, t) = [\kappa_0 (1 - H(t - t_s)) + \kappa_1 H(t - t_s)] \sin\left(2\pi f_s \frac{t}{T} - \frac{z_j}{L} + \varphi\right) \quad (11)$$

where κ_0 and κ_1 are parameters of the model while T is the heart beat cycle. Heaviside function $H(t - t_s)$ is used to simulate the cell repolarization process starting at time t_s, where the cardiac cells recover their potential (T – *wave* in ECG signal). Note that the scaling frequency factor is $f_s \neq 1$ because the mechanical response wave does not have the same frequency with the heart beat. In the model proposed by Eqs. 11, we have assumed that the mechanical activation wave only propagates along the main LV axis (z direction). However,

it is possible to model the wave propagation along the LV circumference by adding further parameters to the functional form of S.

Eqs. 4 to 11 above complete the model for the instantaneous velocity magnitude $v_j(t)$ of each material node. The final step before the three-dimensional LV wall configuration can be updated in time by integrating Eq. 2 is to define the three components of the velocity vector. To do so, we employ an empirical approach for distributing the known velocity magnitude v_j along the three cylindrical coordinate directions as follows:

$$\begin{aligned} v_j^r(t) &= \alpha v_j(t) \\ v_j^\theta(t) &= \beta v_j(t) \\ v_j^\theta(t) &= \gamma v_j(t) \end{aligned} \quad (12)$$

where α,β and γ are parameters of the model satisfying $\alpha^2 + \beta^2 + \gamma^2 = 1$, which are selected as described in the following section.

Calibration of the LV kinematic model—We calibrate the model parameters (i.e α, β, c_0 etc.) and the functional form for $p(t)$ to ensure that the resulting temporal variation of the LV volume $V = V(t)$, dV/dt, agrees with reported values in the literature [44, 35].

We adjust the gross features of dV/dt through the specific functional $p(t)$. In this study, we assume that all material points $j = 1, J_e$ have the same functional form of $p(t)$. During diastole, the LV exhibits a pure elastic expansion (untwist motion). Thus $p(t)$, as a lumped parameter, is allowed to have a (mechanical wave) peak during E-wave filling. The atrial contraction, which induces the LV to expand at late diastole, is also modeled as another (mechanical wave) peak of $p(t)$ during A-wave filling. During systole, the LV depolarization is at work and $p(t)$ variation reflects such electrical activity. The systolic depolarization is simulated with a large positive peak in the variation of $p(t)$ (or the *QRS complex*) [71]. We simulate the potential recovery of the cells (T – *wave* of ECG) [71] by a rapid drop $p(t)$ to zero value at the end of systole.

We fine-tune dV/dt by appropriately adjusting the parameter κ_0 in Eq. 11. The parameters c_0, c_1, c_2, c_3 that appear in Eq. 10 are calibrated around the values reported in the literature for cardiac tissue [66]. The final step is to fine-tune the wall motion by selecting the parameters α, β and γ used to define the components of the velocity vector. These parameters are estimated based on the relative magnitude of the three velocity components obtained from MRI measurements of the velocity of material points on the heart wall [72]. The final values of the various calibrated model parameters are summarized in Table 1 while the calibrated functional form for $p(t)$ is shown in Fig. 8. At the end of systole, we calibrate the LV kinematics via the parameter κ_1 in Eq. 11 so that the total regurgitant flow volume through the BMHV during diastole is approximately 10ml according to the reported in the literature values for St. Jude Regents valve [73], which is the valve we employ in our simulations.

2.2. Fluid-structure interaction numerical method

Governing equations and boundary conditions for fluid domain Ω_f—We treat blood as incompressible, Newtonian fluid with constant viscosity $\nu = 3.33 \times 10^{-6}\ m^2/s$ and specific weight $\rho_f = 1050\ kg/m^3$. These assumptions are widely accepted for blood flow in the heart chamber [21]. The blood motion is governed by the unsteady, three-dimensional Navier-Stokes equations:

$$\begin{aligned} \nabla \cdot \mathbf{u} &= 0 \\ \frac{\partial \mathbf{u}}{\partial t} + \nabla \cdot (\mathbf{u} \otimes \mathbf{u}) &= \nabla \cdot \tau \end{aligned} \quad (13)$$

Where the stress tensor τ relates to the pressure p and strain rate ε via the Newtonian stress-strain relation: $\tau = \frac{-\mathrm{p}}{\rho_f}\mathbf{I} + 2\nu\varepsilon(\mathbf{u})$ and $\varepsilon(\mathbf{u}) = \frac{1}{2}(\nabla u + (\nabla u)^T)$.

As required by the curvilinear immersed boundary (CURVIB) method [1] we employ to solve the governing equations in arbitrarily complex geometries (see subsequent section), Eqs. 13 are formulated in cartesian coordinates and then transformed fully into generalized curvilinear coordinates using the approach proposed by [1]. The CURVIB method is described in more detail in section 2.3.

To solve the Eqs. 13, boundary conditions must be specified on the solid/fluid interface Γ. As seen in Fig. 2, Γ consists of solid surfaces that are either stationary or moving as well as inflow and/or outflow boundaries resulting from truncating the connection of the LV/aorta system we simulate from the rest of the cardiovascular system. Depending on the characteristics of the boundary portion, different strategies are implemented to reconstruct the boundary conditions.

At the mitral inlet Γ_{inlet} (see Fig. 5), we model the mitral valve, which is not included in our simulation, by prescribing a physiologic, time-dependent blood flow flux from the left atrium to the LV chamber as boundary condition $Q_m = Q_m(t)$. The mitral valve is thus assumed to be open at all times but the flux through it varies in time in a manner that mimics the natural pattern during diastole [11, 39] (see Fig. 8). Any spatial variability of the velocity profile at Γ_{inlet} is neglected and the flow is assumed to be uniform at all times.

Outflow boundary conditions need to be imposed at the outflow of the aortic flow track Γ_{outlet}. The flux into the descending aorta Q_a results from the difference between the mitral flux Q_m and the volume rate of change of the LV chamber. That is:

$$Q_a(t) = Q_m(t) - \frac{dV}{dt} \quad (14)$$

This condition needs to be specified at every instant in time for a well-posed incompressible Navier-Stokes problem. For that, at every time-step we obtain the velocity field at Γ_{outlet} by assuming zero velocity gradient normal to the outflow boundary:

$$\frac{\partial \mathbf{u}}{\partial n} = 0 \text{ on } \Gamma_{outlet} \quad (15)$$

and subsequently correct the resulting velocity profile to satisfy Eq. 14 using uniform correction.

Along the Γ_{LV} portion of the boundary, the time-dependent LV wall motion, obtained with the cell-activation method described in section 2.1, is prescribed as input to the simulation and used to drive the LV blood flow. The no-slip and no-flux boundary conditions are imposed for the velocity field at the LV wall portion Γ_{LV} as follows:

$$\mathbf{u}(t) = \mathbf{v}(t) \text{ on } \Gamma_{LV} \quad (16)$$

Along the wall of the aorta domain, which as discussed above is treated as a fixed, rigid boundary, the no-slip and no-flux boundary condition is prescribed by setting:

$$\mathbf{u}(t)=0 \text{ on } \Gamma_{aorta} \quad (17)$$

In our simulations the motion of the BMHV leaflets is driven by the beating left ventricle and, thus, the velocity at the interface between the valve leaflets and the blood flow (Γ_{FSI}) needs to be obtained by a coupled FSI procedure. To find the motion of the BMHV, it is necessary to evaluate the load (moment) applied on the surface of the BMHV leaflets by the blood flow. We can write the fluid solver as an operator F that when acting on the boundary yields the load $\mathbf{M}$ imparted by the fluid on the leaflet surface Γ_{FSI} depending on the boundary and initial conditions on Γ:

$$\mathbf{M}=F(\Gamma) \quad (18)$$

In the next section we describe the equations we solve to determine the motion of the valve leaflets in the FSI algorithm.

Governing equations for solid domain Ω_S—The solid body (i.e the BMHV), whose motion is to be determined by FSI, consists of two leaflets pivoting around their rotational axes under the pulsatile loading of the blood flow (see Fig. 1). The two leaflets are attached via a hinge to a circular housing implanted at the $LVOT$ (see Fig. 5).

The motion of the two leaflets is rigid body rotation around their axes of rotation. In the Cartesian coordinate (X, Y, Z) system shown in Fig. 1, the leaflets rotational axes are parallel to the X direction. We denote with ϕ the opening angle of the leaflet, which can be used to express the position vector ($\mathbf{x}(X, Y, Z)$) of a material point on the leaflet as follows:

$$\mathbf{x}-\mathbf{x}_c=R(\phi)\mathbf{r_c} \quad (19)$$

where $\mathbf{x_c}(X, Y_c, Z_c)$ is the projection of the material point on the rotational axis, $R(\phi)$ is the in-plane rotational matrix (see below), and $\mathbf{r_c}$ is the radial distance to the rotational axis thus: $|r_c|=\sqrt{(Y-Y_c)^2+(Z-Z_c)^2}$. For the specific BMHV we use in our simulations, the maximum angle ϕ_{max} = 58° (fully close) and the minimum angle is ϕ_{min} = 5° (fully open). The in-plane (i.e $X = const$) rotational matrix $R(\phi)$ is defined as follows:

$$R(\phi)=\begin{bmatrix} 1 & 0 & 0 \\ 0 & \cos(\phi) & -\sin(\phi) \\ 0 & \sin(\phi) & \cos(\phi) \end{bmatrix} \quad (20)$$

The governing equation of the leaflet motion is obtained from the conservation of angular momentum and can be written in terms of ϕ as follows:

$$\mathbf{I}_0\frac{\partial^2\phi}{\partial t^2}=\mathbf{M}_0 \quad (21)$$

Here $\mathbf{I}_0$ as the reduced moment of inertia, which is calculated as:

$$\mathbf{I}_0=\frac{\rho_s\int_{\Omega_s}|\mathbf{r_c}|^2dV}{\rho_f D^5} \quad (22)$$

where ρ_s and ρ_f are the specific weight of the solid and fluid, respectively. Finally, M_0 is the moment coefficient:

$$\mathbf{M_0}=\frac{\mathbf{M_x}}{\rho_f U^2 D^3} \quad (23)$$

where $\mathbf{M_X}$ is the moment around the X axis found by integrating the fluid stress τ on the interface Γ_{FSI}

$$\mathbf{M_x}=\int_{\Gamma_{FSI}} \mathbf{r_c} \times \tau dA \quad (24)$$

The structural solver therefore can be written as an operator estimating the position vector **x** (and thus the angle ϕ) from the external load **M** and boundary conditions on Γ_{FSI} asa follows:

$$\phi=S(\Gamma_{FSI}, \mathbf{M}) \quad (25)$$

The Fluid-Structure Interaction algorithm to calculate the motion of Γ_{FSI}—The details of fluid-structure interaction algorithms are presented in [2] and thus only a brief description of the method is discussed here. The kinematics of the leaflets of BMHV is the result of the interaction between the blood flow dynamics in the LVOT and the inertia of the leaflets. In our partition approach (Dirichlet-Neumann) FSI approach, the load (M) is calculated from the fluid solver (F) and is prescribed as Neumann boundary condition for the structure solver (S). The structural solver is then used to find the position of the leaflets, which is prescribed as Dirichlet boundary conditions for the fluid solver. The kinematic condition requires the continuity of the interface between solid and fluid (see Fig. 2):

$$\Gamma_s \equiv \Gamma_f \equiv \Gamma_{FSI} \quad (26)$$

Note that the solid/fluid boundary, which consists of the fluid-structure interaction interface Γ_{FSI}, is also a function of the leaflet angle ϕ. Therefore we can write:

$$\Gamma_{FSI}=\Gamma(\phi) \quad (27)$$

The dynamic condition requires the continuity of the stress at the interface:

$$\tau_f=\tau_s \quad (28)$$

with no the slip condition on the interface Γ_{FSI}:

$$\mathbf{v}_s=\mathbf{u}_f \quad (29)$$

The governing equations for the fluid (F) and solid (S) parts presented in the previous sections can now be combined and expressed in operator form as follows:

$$\mathbf{M}=F(\Gamma(\phi)) \quad (30)$$

$$\phi=S(\Gamma(\phi), \mathbf{M}) \quad (31)$$

Note that the operators S and F change with time and are dependent on the initial and boundary conditions imposed on the boundary Γ. Thus this system of equations can be written in compact notation:

$$\phi=S \circ F(\phi) \quad (32)$$

where the operator ○ denotes the transfer load at the interface Γ_{FSI} from the fluid solver to the solid solver and supply for the solid solver $S = S(\mathbf{M})$. Therefore, the coupling between the solid solver S and the fluid solver F is equivalent to finding the fixed point of the operator $S \circ F$.

Assuming that the leaflet angle ϕ is known at time step $n - 1$, we solve Eqn. 32 to obtain the leaflet angle at timestep n with the current boundary conditions on Γ via a series of strong-coupling sub-iterations [2]. The Aitken non-linear relaxation technique is used to accelerate convergence and enhance robustness [2, 74]. For more details, the reader is referred to [2].

2.3. Discretization and numerical integration

The numerical method for solving the governing equations combines the CURVIB method with overset grids as shown in Fig. 2. The computational domain is decomposed into two overlapping blocks. The first block contains the left ventricle. The moving LV geometry is embedded in a stationary background curvilinear mesh, which outlines but does not conform with the LV wall, and treated as a sharp-interface immersed boundary using the CURVIB approach to effiectively handle the large wall deformation. The second block motion consists of the aortic arch, which is discretized with a boundary fitted curvilinear mesh. The BMHV leaflets are embedded in the background aorta mesh and treated as immersed boundaries via the CURVIB method. The overlapping interfaces of the LV and aorta sub-domains are $\Gamma^{LV}_{interface}$ and $\Gamma^{aorta}_{interface}$, respectively. The governing equations are solved in each sub-domain (see Fig. 5) using the sharp-interface curvilinear-immersed boundary (CURVIB) method of [1] (see below). Tri-linear interpolation is used to reconstruct boundary conditions at each node on the overlapping interface using the 8 grid points of the neighboring sub-domain surrounding the node at the interface of the host sub-domain. The details of the numerical method can be found in [75].

The central part of the CURVIB method is the reconstruction of boundary conditions for the velocity field [76] at grid nodes in the immediate vicinity of the boundary. The reconstruction is either linear or quadratic interpolation along the local normal to the solid body [76]. The governing equations are discretized on a hybrid staggered-non-staggered grid, which facilitates both the boundary condition reconstruction process as well as the enforcement of the discrete divergence-free constraint [57]. We use the 2^{nd} order accurate QUICK scheme for the convective terms and three-point, second-order accurate, central differencing for all other terms. For time integration, we employ a second-order accurate fractional step methodology [1]. A Newton-Krylov solver is used to solve the non-linear discrete momentum equations in the momentum step and a GMRES solver with multigrid preconditioner is employed for the Poisson equation in the projection step. The CURVIB method has been shown to be 2^{nd} order accurate in space and time [57, 1]. The details of the FSI solver can be found in [2] and [75].

The FSI-CURVIB flow solver has been extensively validated in [2] for pulsatile flow past a BMHV in a straight, axisymmetric aorta and under physiologic conditions. In that work, the computed results were compared with particle-image velocimetry (PIV) and leaflet kinematics measurements [15] and were shown to be in very good agreement. More recently, we have also demonstrated the ability of the method to capture very complex vortex dynamics in impulsively driven flow through an inclined nozzle [77]. Le et al. [77] showed that the simulations, carried out with the same numerical method we employ herein, are in excellent agreement with the measurements [78, 79]. The inclined nozzle test case is relevant to the simulations presented in this paper in so far as it is characterized by the formation and instability of an inclined and asymmetric vortex ring, which, as we will subsequently show, also dominates the LV flow during diastolic filling.

2.4. Computational setup

As shown in Fig. 5, the LV and aorta sub-domains are discretized with grids consisting of 161 × 281 × 161 and 161 × 161 × 401 nodes, respectively. As discussed above, the grid discretizing the LV sub-domain is a stationary curvilinear mesh that contains at all times but does not conform to the LV wall. The aorta mesh is a boundary-conforming curvilinear mesh. In the overlap region of the two sub-domains, the aorta block is extended along its longitudinal axis $0.55D$ into the left ventricle block, where D is the aorta diameter at the LVOT. The LV wall is discretized with an unstructured triangular mesh, as required by the CURVIB method, with 3648 nodes as shown in Fig. 4. The BMHV leaflets are also discretized with an unstructured mesh, with 104 nodes on each leaflet as seen in Fig. 1.

The heart beat cycle T is chosen to correspond to a heart rate of 52 bpm, $T = 1.15s$. The systolic rate, ie. the ratio of the systole duration over the cardiac cycle, is chosen to be 40% as in the normal range [80]. The systolic rate is set by allocating the length of systolic and diastolic activation period of $p(t)$ correspondingly. The simulation time step is $\Delta t = 0.1074$ ms, which corresponds to discretizing the cardiac cycle with $N = 10710$ time steps.

The valve is chosen as St. Jude Regent 23mmm implanted in the cusp-noncusp plane of the aortic root. The symmetric plane ($x = 0$) of the BMHV nearly goes through the apex of the LV chamber (see Fig. 5). The leaflet density of $\rho_s = 1750 kg/m^3$ (Polycarbonate) and fluid density of $\rho_f = 1000 kg/m^3$ in this case resulting I_0 of 0.001 (see Eqn. 22 for the definition of I_0).

3. Results and discussion

In this section we present the results of our computational model and discuss their physiologic significance. We begin by demonstrating the ability of the model we developed for animating the LV wall to yield kinematics that are well within the physiologic range for a human subject. Subsequently we discuss the calculated hemodynamics during diastole and systole and the leaflet kinematics that result from the FSI simulation of the BMHV driven by the cell-based activation model for the wall motion.

LV wall kinematics

To demonstrate that the emerging, large-scale LV wall kinematics resulting from the proposed model is physiologic, major global LV kinematics parameters calculated from the model are summarized in Table 2. The most important parameter during diastole is the E-wave velocity at the mitral orifice. In our case, the E-wave peak velocity, which is estimated as the bulk velocity from the mitral inflow wave from, reaches 70 cm/s. This value is in the range of measurements obtained from *in vivo* MRI, which range from 50 to 70 cm/s [81, 41, 38]. The variation of the LV volume over one cardiac cycle (expansion during diastole and contraction during systole) is typically quantified in terms of its minimum (end systolic volume or ESV) and maximum (end diastolic volume or EDV). The stroke volume (SV) is defined as the difference of these two values, i.e. SV = EDV-ESV, and the ejection fraction (EF) is defined as EF=SV/EDV. The values for all these important quantities for characterization the ventricular function summarized in Table 2 are well within the physiologic range for a normal subject [82]. For example, the range of values for EF observed $in-vivo$ is from 40% to 60% [82].

The instantaneous direction of the calculated wall velocity field is visualized in Fig. 6 in terms of instantaneous LV wall streamlines at several instants during the cardiac cycle. The velocity field is given by Eqs. 2 to 12 with the model parameters summarized in Table 1. As seen in Fig. 6, the cell-activation model produces wall surface motion that exhibits complex twisting motion as it relaxes in the clockwise direction (looking from the base) during

diastole and contracts in the counter-clockwise direction during systole. These twisting patterns are consistent with *in vivo* observations [21], in which the rotation of the apex relative to the base is in the counter-clockwise direction during systole and clockwise during diastolic untwist (as viewed from the base).

To quantify the local deformation of the LV wall, we track the motion of one material point (see Fig. 4 for its location) on the LV wall by plotting time series of the three velocity components at this point in Fig. 7. During the rapid filling phase (E-wave) the material point rapidly moves toward the apex as indicated by the large positive spike in the longitudinal velocity ($\upsilon^{z}_{max} \approx 8\ cm/s$). At the same time the LV chamber expands at lower rate ($\upsilon^{r}_{max} \approx 4\ cm/s$) and twists around the LV axis ($\upsilon^{\theta}_{max} \approx 8\ cm/s$). During systole, the wall motion exhibits radial, longitudinal and twisting motions with velocities in the range of 3 − 4 cm/s.

As shown in Fig. 7, the magnitude and direction of the velocity resulting from our model exhibits wide variations from diastole to systole in a manner that closely resembles $in-vivo$ data reported in [72, 83]. During the rapid filling phase (E-wave) the endocardium motion resulting from our model is in good quantitative agreement with the MRI tissue phase mapping data [84, 85], which report the radial expansion velocity in the range of 4-5 cm/s and longitudinal velocity of 10 cm/s. During systole, the wall motion exhibits radial, longitudinal and twisting motions with velocities of 3 – 4 cm/s, which also agree with the reported values (3-5 cm/s) in the literature [84].

The calculated LV volume rate of change dV/dt during one cardiac cycle is shown in Fig. 8. During diastole, the distinct early diastolic filling peak (E-wave) is separated from the passive filling peak (A-wave) by a phase of very slow volume expansion, referred to as diastasis. An important physiologic parameter is the ratio of the E- and A-waves dV/dt peaks (E/A ratio). As shown in Fig. 8, the E/A ratio resulting from our model is approximately 1:1, which is in good agreement with physiologic values [86, 87, 88].

In the systolic phase, the dV/dt resulting from the model becomes as low as $-19\ liter/min$ (see Fig. 8), which is also well within the physiologic in the order of $-20\ liter/min$ [73, 19]. At the end of the cardiac cycle, and as seen in Fig. 8, the LV chamber exhibits a slight expansion. This is due to the fact that the flow in the ascending aorta exhibits slightly reverse regurgitant flow. This behavior is entirely consistent with what has been observed in a number of *in vivo* studies [89, 90, 88].

It is important to re-emphasize that the LV volume rate of change as well as all LV kinematic parameters presented above are driven in our model by the transmembrane potential $p(t)$, which is also shown in Fig. 8. Our main assumption is that the $p(t)$, which is similar to surface potential obtained from surface ECG as discussed above, implicitly reflects the dynamics of the LV wall [71, 91, 69]. In this sense, $p(t)$ in our model can be viewed as emerging from electrical activity of many cells. The electrical potential has the largest depolarization peak at systole (QRS complex of ECG). In the E-wave filling period, however, the LV chamber exhibits a pure elastic expansion and thus ECG signal does not reflect such elastic expansion. To mimic the expansion wave, the variation of $p(t)$ during E-wave is allowed to exhibit an elastic excitation peak $p(t)$ in Fig. 8 to mimic such pure mechanical behavior. During A-wave filling, the atrium contracts under its depolarization (P-wave of ECG signal) [71] and induces the LV to expand. This A-wave period of LV is also represented by a smaller peak in the variation of $p(t)$ as shown in Fig. 8.

Finally, there are two important non-dimensional numbers, which control the large scale intraventricular hemodynamics. Namely, the peak systolic Reynolds number (Re) and the

Womersley number (W_o). Using the aortic diameter $D = 26.7\ mm$, peak systolic bulk velocity $U_0 = 0.55\ m/s$ and heart beat cycle $T = 1.15 s$ as the length, velocity and time scales, these parameters and their values resulting from our model are given as follows:

$$\begin{aligned} W_o &= \sqrt{\frac{D^2}{T\nu}} \approx 13.6 \\ Re_D &= \frac{U_0 \cdot D}{\nu} \approx 4383 \end{aligned} \quad (33)$$

Both of these values are well within the physiologic regime [81, 9].

In summary, the results we have presented in this section make a strong case that the model we developed in this work to animate the LV wall yields kinematics that are well within the physiologic range. These include not only essentially all significant global LV parameters but also the qualitative and quantitative variation of the endocardium velocity field throughout the cardiac cycle.

LV hemodynamics

During the diastolic phase the intraventricular flow is dominated by the rapid filling of blood flow from the left atrium into the left ventricular chamber. The calculated vortex dynamics during the filling phase is visualized in Fig. 9 by plotting out-of-plane instantaneous vorticity contours on the vertical plane of symmetry of the BMHV leaflets ($x = 0$ plane).

The initial flow structure is organized and laminar with the high velocity front propagating impulsively downstream of the mitral orifice to create a mitral vortex ring as seen in Fig. 9a. The asymmetric LV geometry induces the ring to become inclined and asymmetric. As clearly seen in Fig. 9a, a large vortex core is formed near the LVOT cavity while the ring core near the posterior wall is significantly smaller.

It should be noted that during the diastolic phase, the BMHV leaflets, while free to move and interact through the FSI algorithm with the blood flow, remain closed and stationary as seen in Fig. 9. There is, however, a small amount of leakage flow near the edges of the leaflet as shown in Fig. 9a. The leakage flow forms because when a BMHV is implanted the leaflets in the fully-closed position are not in complete contact with the housing wall but instead a small gap exists between the edge of the leaflet the aorta wall [92]. A small but intense jet (known as the periphery jet [92]) forms through this gap region and dissipates quickly into the central region of the aortic valve. Our results show that even though very small, this leakage flow interferes significantly with the formation of the mitral vortex ring during diastole and causes the ring to break up close to the mitral orifice as shown in Fig. 9a and b.

At the end of E-wave, the core of the mitral vortex ring has broken up into small scale structures occupying the central region of the LV chamber (see Fig. 9b). Such structures continue to propagate toward the posterior wall and the LV apex during diastasis as seen in Fig. 9c. After the A-wave passive filling, the blood flow rolls up again at the edge of the mitral orifice to create additional vortex cores. Since the peak and the duration of A-wave are significantly smaller than the E-wave, these vortex cores stay close to the mitral orifice and do not propagate far into the LV chamber as shown in Fig. 9d. At the end of diastole, small scale structures fill up the entire LV chamber.

The systolic phase starts with the contraction of the left ventricle and the small scale flow structures are ejected from the LV chamber into the aorta. During the opening of the BMHV, the flow accelerates rapidly from the apex towards the septum wall and across the valve as shown in Fig. 10a. Shear layers start to develop inside the LVOT at the two side

orifices, forming between the housing wall and the leaflets, as well as the central orifice between the two leaflets as shown in Fig. 10b. It is important to note that these shear layers and the associated roll-up of the flow downstream of the leaflets are broadly similar to those observed in previous simulations and experiments with a BMHV in a straight axi-symmetric aorta [15]. Our results do show, however, that in the anatomic case the shear-layer formation is impacted by interactions with small-scale flow structures that are advected by the accelerating systolic flow from the LV chamber past the valve leaflets. Moreover, the flow is seen to separate from the housing area near the upper leaflet causing a clearly defined shear layer of positive vorticity at peak systole (see Fig. 10b).

As the LV continues to contract, the vortical structures shed from the valve leaflets advance toward the aortic root and break up rapidly into a turbulent-like state past peak systole as seen in 10c. At the end of systole, the LV slightly expands (see Fig. 8) and the aortic flow exhibits reverse flow. The retrograde flow from the aorta drives the leaflets swiftly to the fully close position as shown in Fig. 10d. As seen in the figure, the closing of the valve is asymmetric with the lower leaflet closing faster than the upper one. In fact, the acceleration of the lower leaflet is sufficiently large to induce a high speed leakage jet in the region between the leaflet edge and the aortic wall as shown in Fig. 10d. This high speed jet penetrates back into the LV chamber as the BMHV approaches fully close state as seen in Fig. 10d.

The formation of the mitral vortex ring during E-wave filling has been confirmed in previous studies both *in–vivo* [88, 6] and computational studies [93, 39, 38, 28]. Our findings on the formation of the vortex ring at the mitral orifice during E-wave agree well with *in – vivo* measurement [88, 94, 3, 6] and other computational works [42, 39, 45, 44, 40, 38, 28]. Our result in Fig. 9a further shows that the vortex ring is highly asymmetrical with the vortex core at the anterior side (aortic side) is larger than the posterior side. This feature agrees with recent three-dimensional measurements from MRI data [6] where the mitral vortex is shown to be an inclined vortex ring in healthy subjects.

The evolution of the mitral vortex ring in Figs. 9a-d is the result of both self-deformation of the mitral vortex ring and its interaction with the left ventricular wall. Moreover, our result in Fig. 9b suggests that the break up of the mitral valve vortex ring is an important phenomenon since the so resulting small-scale flow patterns dominate the flow field inside the LV chamber through out the subsequent systolic phase. Finally, the large scale rotational direction of LV flow at the end of diastole in Fig. 9d is consistent with *in – vivo* measurements in healthy subjects [95, 6], in which the asymmetrical evolution of the mitral vortex ring set up the clockwise rotational pattern at the end of diastole. For further discussion of the mitral vortex ring evolution, the reader is referred to [96].

The three-dimensional structure of the intraventricular flow is visualized in Fig. 11 by plotting instantaneous iso-surface of Q-criteria [97] at four instances during the cardiac cycle. The formation of the asymmetric, donut-shaped, mitral vortex ring at the end of the E-wave filling is clearly evident in Fig. 11a. The mitral vortex ring is initially inclined at an angle to the mitral annulus as its two sides propagate at different speeds into the LV chamber. The coherence of mitral vortex ring is rapidly lost as it breaks down into small scale structures due to three-dimensional instabilities and its interaction with the LV wall as seen in Fig. 11b.

The three-dimensional structure of the flow during systole is visualized in Figs. 11c and d. The existence of worm-like, coherent structures inside the LV chamber at the beginning of systole is shown in Fig. 11c. These structures are circulated within the LV by the clockwise rotational flow during early systole and subsequently ejected rapidly toward the LVOT. As

the LV contraction progresses, these structures are elongated and stretched as they are transported through the LVOT past the two leaflets. At peak systole, the flow downstream of the leaflets exhibits is explosive, small-scale dynamics dynamics as the large-scale coherent structures break down into a turbulent-like state filling the entire aortic root region (see Fig. 11c). After the BMHV closes fully, the coherent structures inside the aorta dissipate quickly and the flow returns to rest at the end of cardiac cycle as shown in Fig. 11d.

Our results in Fig. 11 reveal, for the first time, the existence of the complex coherent structures at the $LVOT$ during systole. Simulations with idealized left heart models [46] suggest that the complex geometry of the LV chamber and the curvature of the aorta induce the flow to form a large scale three dimensional swirling flow [46]. The presence of large scale three-dimensional coherent structures has also been confirmed via $in-vivo$ measurements in healthy volunteer [6]. However, the formation of the small scale structures, which are created during diastole as seen in Fig. 9b and Fig. 11b and convected out to the $LVOT$ during systole, has never been uncovered both experimentally and numerically before. The existence of these small scale structures are important because they interact with the upper leaflet as seen in Fig. 10b and affect the leaflet dynamics. Since the leaflet dynamics control the three dimensional vortex shedding from the leaflet surface and the housing as seen in Fig. 10b, controlling the small scale structures is important for prosthetic heart valve design.

The leaflet kinematics

The calculated kinematics of the BMHV leaflets are shown in Fig. 12 in terms of the temporal variation of the angle of each leaflet ϕ. As seen in this figure, both the upper (leaflet 1) and lower (leaflet 2) leaflets accelerate rapidly and almost simultaneously during the opening phase, which is symmetric (in the sense that both leaflets open at the same time) and lasts about 50-70 ms. Asymmetries in the motion of the two leaflets are observed, however, as the leaflets reach the fully open position. In particular, and as shown in the zoomed-in view of Fig. 12, leaflet 2 is clearly seen to decelerate faster than leaflet 1. The zoomed-in view in Fig. 12 also shows that both leaflets rebound slightly after they reach the fully opening position.

The BMHV remains fully open for about 400 ms and only starts to close when significant reverse flow develops in the aorta. The closing phase occurs in about 80 ms. Unlike the opening phase, however, the closing is highly asymmetric with leaflet 2 closing faster than leaflet 1 (see Fig. 12). The large asymmetry of the leaflet kinematics is due to the three-dimensional anatomic geometry but also the interaction of the highly three-dimensional retrograde flow coming back into the left ventricle and the leaflets as seen in Fig. 10d. Since most of the retrograde flow is directed toward the lower part of the LV, leaflet 2 tends to close faster than leaflet 1.

After reaching the fully close position, leaflet 2 rebounds for about 40ms before coming back to fully close position. This complex dynamic response of leaflet 2 is the main culprit for the high speed jet observed in Fig. 10d in the gap between the edge of leaflet 2 and the housing area.

The calculated kinematics of the leaflets in our simulation exhibit similarities but also significant differences with previous simulations in straight and anatomic aorta geometries in which the valve motion is driven by a pulsatile wave form [16, 2, 56]. The large asymmetries during the closing phase found in our simulations are in stark contrast with the symmetric leaflet motion documented in experiments and simulations for a straight, axi-symmetric aorta geometry [15]. The delay in the opening of leaflet 2 observed in our simulations is similar to that observed in the simulations of [56] who used an anatomic aorta

with a prescribed wave form at the inlet of the aorta. The leaflet rebound after the leaflets reach the fully open position has also been reported previously in both idealized aorta [2] and anatomic geometries [56] and is consistent with $in-vitro$ experimental data of [15]. In summary, our results along with the previous simulations of [98] clearly show that the anatomical geometry of the aorta and the implantation orientation of the BMHV can significantly alter the flow dynamics and the leaflet kinematics.

4. Conclusions and future directions

We developed a novel cell-activation based model for simulating physiologic kinematics of the left ventricle. The model is inspired by cardiac electro-physiology and gives rise to physiologic large-scale kinematics of the endocardium as a function of a time-dependent transmembrane potential. We showed that the model not only simulates physiologic global LV parameters but also gives rise to large-scale contractile mechanisms that can simulate the effect of fiber expansion, contraction and twist.

The model of the LV wall motion was used to drive the large-scale FSI between the blood flow and the leaflets of a BMHV implanted in the aortic position. To our knowledge this is the first time that the motion of a valve prosthesis is simulated in an anatomic LV/aorta model driven by a contracting ventricle. Our simulations captured the formation and break up of the mitral vortex ring during diastole and showed that the leakage jet flow emanating from the gaps between the leaflet edges and the aortic wall can disrupt and destabilize the LV flow during diastolic filling even when the valve is in the closed position. During systole, our simulations revealed the symmetric opening of the two leaflets and small asymmetric rebound as the leaflets approach the fully open position. The valve closing phase, however, exhibits highly asymmetric kinematics induced by the complexity of the anatomic geometry and the three-dimensionality of the retrograde flow that enters the LV chamber from the aorta.

The time-dependent transmembrane potential ($p(t)$) that drives the LV wall motion in our model is obtained in the present work through calibration to ensure physiologic LV motion. In future extension of the model, the value of $p(t)$ may be calibrated to develop a range of beating LV models for both healthy and diseased hearts.

The LV/aorta system is truncated from the whole arterial tree and the motion of the valve leaflets are driven by the beating left ventricle only. Thus the effect of the rest of the cardiovascular system, such as flow resistance arising from smaller arteries such as the carotid arteries, subclavian arteries at the descending aorta, is not included. These resistances, which play an important role in regulating the valve closure, are patient-specific and are not known in advance. In future studies, our computational model can be extended to incorporate one-dimensional resistance models [99] that can account for such effects.

The presence of a native or prosthetic valve in the mitral position is not simulated in our model and thus mitral valve effects are not accounted for. Recent works [93, 38, 33], however, have clearly shown the importance of the prosthetic mitral valve on the LV hemodynamics. Our future work will thus focus on extending our computational framework to develop FSI modules for simulating native and various prosthetic heart valves, such that the complete LV/aorta system with valves both in the aortic and mitral positions can be simulated.

Acknowledgments

This work was supported by NIH Grant RO1-HL-07262 and the Minnesota Supercomputing Institute. We would like to thank Professor Ajit Yoganathan and his associates for providing us the anatomic geometry of the left

ventricle. We also acknowledge the help of Professor Iman Borazjani in implementing the domain decomposition aspects of the numerical method. The first author was supported partially by a fellowship from Vietnam Education Foundation.

References

1. Ge L, Sotiropoulos F. A numerical method for solving the 3d unsteady incompressible navier-stokes equations in curvilinear domains with complex immersed boundaries. Journal of Computational Physics. 2007; 225(2):1782. [PubMed: 19194533]
2. Borazjani I, Ge L, Sotiropoulos F. Curvilinear immersed boundary method for simulating fluid structure interaction with complex 3d rigid bodies. Journal of Computational Physics. 2008; 227(16):7587–7620. [PubMed: 20981246]
3. Hong G-R, Pedrizzetti G, Tonti G, Li P, Wei Z, Kim JK, Baweja A, Liu S, Chung N, Houle H, Narula J, Vannan MA. Characterization and Quantification of Vortex Flow in the Human Left Ventricle by Contrast Echocardiography Using Vector Particle Image Velocimetry. J Am Coll Cardiol Img. 2008; 1(6):705–717.
4. Lee J, Niederer S, Nordsletten D, Le Grice I, Smail B, Kay D, Smith N. Coupling contraction, excitation, ventricular and coronary blood flow across scale and physics in the heart. 2009; 367(1896):2311–2331.
5. Faludi R, Szulik M, D'hooge J, Herijgers P, Rademakers F, Pedrizzetti G, Voigt J-U. Left ventricular flow patterns in healthy subjects and patients with prosthetic mitral valves: An in vivo study using echocardiographic particle image velocimetry. J Thorac Cardiovasc Surg. 2010; 139(6): 1501–1510. [PubMed: 20363003]
6. Markl M, Kilner P, Ebbers T. Comprehensive 4d velocity mapping of the heart and great vessels by cardiovascular magnetic resonance. Journal of Cardiovascular Magnetic Resonance. 2011; 13(1):7. [PubMed: 21235751]
7. Kvitting J-PE, Dyverfeldt P, Sigfridsson A, Franzén S, Wigström L, Bolger AF, Ebbers T. In vitro assessment of flow patterns and turbulence intensity in prosthetic heart valves using generalized phase-contrast mri. Journal of Magnetic Resonance Imaging. 2010; 31(5):1075–1080. [PubMed: 20432341]
8. Pierrakos O, Vlachos PP, Telionis DP. Time-resolved dpiv analysis of vortex dynamics in a left ventricular model through bileaflet mechanical and porcine heart valve prostheses. Journal of Biomechanical Engineering. 2004; 126(6):714–726. [PubMed: 15796330]
9. Cenedese A, Del Prete Z, Miozzi M, Querzoli G. A laboratory investigation of the flow in the left ventricle of a human heart with prosthetic, tilting-disk valves. Experiments in Fluids. 2005; 39:322–335.
10. Pierrakos O, Vlachos PP. The effect of vortex formation on left ventricular filling and mitral valve efficiency. Journal of Biomechanical Engineering. 2006; 128(4):527–539. [PubMed: 16813444]
11. Querzoli G, Fortini S, Cenedese A. Effect of the prosthetic mitral valve on vortex dynamics and turbulence of the left ventricular flow. Physics of Fluids. 2010; 22(4):041901.
12. Hart JD, Peters G, Schreurs P, Baaijens F. A two-dimensional fluid-structure interaction model of the aortic value. Journal of Biomechanics. 2000; 33(9):1079–1088. [PubMed: 10854880]
13. Hart JD, Baaijens FPT, Peters GWM, Schreurs PJG. A computational fluid-structure interaction analysis of a fiber-reinforced stentless aortic valve. Journal of Biomechanics. 2003; 36(5):699–712. cardiovascular Biomechanics. [PubMed: 12695000]
14. van Loon R, Anderson PD, de Hart J, Baaijens FPT. A combined fictitious domain/adaptive meshing method for fluidstructure interaction in heart valves. International Journal for Numerical Methods in Fluids. 2004; 46(5):533–544.
15. Dasi LP, Ge L, Simon HA, Sotiropoulos F, Yoganathan AP. Vorticity dynamics of a bileaflet mechanical heart valve in an axisymmetric aorta. Physics of Fluids. 2007; 19(6):067105.
16. De Tullio MD, Cristallo A, Balaras E, Verzicco R. Direct numerical simulation of the pulsatile flow through an aortic bileaflet mechanical heart valve. Journal of Fluid Mechanics. 2009; 622:259–290.

17. Griffith BE. Immersed boundary model of aortic heart valve dynamics with physiological driving and loading conditions. International Journal for Numerical Methods in Biomedical Engineering. 2011:n/a–n/a.
18. Borazjani I, Ge L, Sotiropoulos F. High-resolution fluid structure interaction simulations of flow through a bi-leaflet mechanical heart valve in an anatomic aorta. Annals of Biomedical Engineering. 2010; 38:326–344. [PubMed: 19806458]
19. Yoganathan A, Chandran K, Sotiropoulos F. Flow in prosthetic heart valves: State-of-the-art and future directions. Annals of Biomedical Engineering. 2005; 33:1689–1694. [PubMed: 16389514]
20. Ge L, Sotiropoulos F. Direction and magnitude of blood flow shear stresses on the leaflets of aortic valves: Is there a link with valve calcification? Journal of Biomechanical Engineering. 2010; 132(1):014505. [PubMed: 20524753]
21. Hunter PJ, Pullan AJ, Smaill BH. Modeling total heart function. Annual Review of Biomedical Engineering. 2003; 5(1):147–177.
22. Nordsletten D, Niederer S, Nash M, Hunter P, Smith N. Coupling multi-physics models to cardiac mechanics. Progress in Biophysics and Molecular Biology. 2011; 104(1-3):77–88. cardiac Physiome project: Mathematical and Modelling Foundations. [PubMed: 19917304]
23. Dominguez G, Fozzard HA. Effect of stretch on conduction velocity and cable properties of cardiac purkinje fibers. American Journal of Physiology - Cell Physiology. 1979; 237(3):C119–C124.
24. Sengupta PP, Khandheria BK, Korinek J, Wang J, Jahangir A, Seward JB, Belohlavek M. Apex-to-Base Dispersion in Regional Timing of Left Ventricular Shortening and Lengthening. J Am Coll Cardiol. 2006; 47(1):163–172. [PubMed: 16386681]
25. Nash M, Hunter P. Computational mechanics of the heart. Journal of Elasticity. 2000; 61:113–141.
26. Noble D. Modeling the heart–from genes to cells to the whole organ. Science. 2002; 295(5560): 1678–1682. [PubMed: 11872832]
27. Kovacs SJ, Mcqueen DM, Peskin CS. Modelling cardiac fluid dynamics and diastolic function. Philosophical Transactions of the Royal Society of London. Series A: Mathematical, Physical and Engineering Sciences. 2001; 359(1783):1299–1314.
28. Krittian S, Janoske U, Oertel H, Böhlke T. Partitioned fluidGsolid coupling for cardiovascular blood flow. Annals of Biomedical Engineering. 2010; 38:1426–1441. [PubMed: 20058187]
29. Arts T, Reneman RS, Veenstra PC. A model of the mechanics of the left ventricle. Annals of Biomedical Engineering. 1979; 7:299–318. [PubMed: 547767]
30. Beyar R, Sideman S. The dynamic twisting of the left ventricle: A computer study. Annals of Biomedical Engineering. 1986; 14:547–562. [PubMed: 3826804]
31. Yellin EL, Meisner JS. Physiology of diastolic function and pressure-flow relations. Cardiology Clinics. 2000; 18(3):411–433. [PubMed: 10986581]
32. Thomas J, Weyman A. Numerical modeling of ventricular filling. Annals of Biomedical Engineering. 1992; 20:19–39. [PubMed: 1562102]
33. Kim H, Vignon-Clementel I, Figueroa C, LaDisa J, Jansen K, Feinstein J, Taylor C. On coupling a lumped parameter heart model and a three-dimensional finite element aorta model. Annals of Biomedical Engineering. 2009; 37:2153–2169. [PubMed: 19609676]
34. Vierendeels JA, Riemslagh K, Dick E, Verdonck PR. Computer simulation of intraventricular flow and pressure gradients during diastole. Journal of Biomechanical Engineering. 2000; 122(6):667–674. [PubMed: 11192390]
35. Baccani B, Domenichini F, Pedrizzetti G, Tonti G. Fluid dynamics of the left ventricular filling in dilated cardiomyopathy. Journal of Biomechanics. 2002; 35(5):665–671. [PubMed: 11955506]
36. Baccani B, Domenichini F, Pedrizzetti G. Model and influence of mitral valve opening during the left ventricular filling. Journal of Biomechanics. 2003; 36(3):355–361. [PubMed: 12594983]
37. Domenichini F, Pedrizzetti G, Baccani B. Three-dimensional filling flow into a model left ventricle. Journal of Fluid Mechanics. 2005; 539:179–198.
38. Schenkel T, Malve M, Reik M, Markl M, Jung B, Oertel H. Mri-based cfd analysis of flow in a human left ventricle: Methodology and application to a healthy heart. Annals of Biomedical Engineering. 2009; 37:503–515. [PubMed: 19130229]

39. Saber NR, Wood NB, Gosman AD, Merrifield RD, Yang G-Z, Charrier CL, Gatehouse PD, Firmin DN. Progress towards patient-specific computational flow modeling of the left heart via combination of magnetic resonance imaging with computational fluid dynamics. Annals of Biomedical Engineering. 2003; 31:42–52. [PubMed: 12572655]
40. Long Q, Merrifield R, Xu XY, Kilner P, Firmin DN, Yang GZ. Subject-specific computational simulation of left ventricular flow based on magnetic resonance imaging. Proceedings of the Institution of Mechanical Engineers, Part H: Journal of Engineering in Medicine. 2008; 222:475–485.
41. Saber N, Gosman A, Wood N, Kilner P, Charrier C, Firmin D. Computational flow modeling of the left ventricle based on in vivo mri data: Initial experience. Annals of Biomedical Engineering. 2001; 29:275–283. [PubMed: 11339325]
42. Lemmon JD, Yoganathan AP. Three-dimensional computational model of left heart diastolic function with fluid–structure interaction. Journal of Biomechanical Engineering. 2000; 122(2): 109–117. [PubMed: 10834150]
43. McQueen DM, Peskin CS. A three-dimensional computer model of the human heart for studying cardiac fluid dynamics. SIGGRAPH Comput Graph. 2000; 34:56–60.
44. Cheng Y, Oertel H, Schenkel T. Fluid-structure coupled cfd simulation of the left ventricular flow during filling phase. Annals of Biomedical Engineering. 2005; 33:567–576. [PubMed: 15981858]
45. Watanabe H, Sugiura S, Kafuku H, Hisada T. Multiphysics simulation of left ventricular filling dynamics using fluid-structure interaction finite element method. Biophysical Journal. 2004; 87(3):2074–2085. [PubMed: 15345582]
46. Nakamura M, Wada S, Yamaguchi T. Computational analysis of blood flow in an integrated model of the left ventricle and the aorta. Journal of Biomechanical Engineering. 2006; 128(6):837–843. [PubMed: 17154683]
47. Vigmond EJ, Clements C, McQueen DM, Peskin CS. Effect of bundle branch block on cardiac output: A whole heart simulation study. Progress in Biophysics and Molecular Biology. 2008; 97(2-3):520–542. life and Mechanosensitivity. [PubMed: 18384847]
48. Tang, D.; Yang, C.; Geva, T.; del Nido, PJ. Image-based patient-specific ventricle models with fluid-structure interaction for cardiac function assessment and surgical design optimization. Progress in Pediatric Cardiology; proceedings of the 1st International Conference on Computational Simulation in Congenital Heart Disease; 2010. p. 51-62.
49. Peskin CS. Flow patterns around heart valves: A numerical method. Journal of Computational Physics. 1972; 10(2):252–271.
50. Peskin CS. Numerical analysis of blood flow in the heart. Journal of Computational Physics. 1977; 25(3):220–252.
51. Peskin CS, McQueen DM. A three-dimensional computational method for blood flow in the heart i. immersed elastic fibers in a viscous incompressible fluid. Journal of Computational Physics. 1989; 81(2):372–405.
52. McQueen DM, Peskin CS. A three-dimensional computational method for blood flow in the heart. ii. contractile fibers. Journal of Computational Physics. 1989; 82(2):289–297.
53. Sotiropoulos F, Borazjani I. A review of state-of-the-art numerical methods for simulating flow through mechanical heart valves. Medical and Biological Engineering and Computing. 2009; 47:245–256.10.1007/s11517-009-0438-z [PubMed: 19194734]
54. Cheng R, Lai YG, Chandran KB. Three-dimensional fluid-structure interaction simulation of bileaflet mechanical heart valve flow dynamics. Annals of Biomedical Engineering. 2004; 32:1471–1483. [PubMed: 15636108]
55. Ge L, Leo H-L, Sotiropoulos F, Yoganathan AP. Flow in a mechanical bileaflet heart valve at laminar and near-peak systole flow rates: Cfd simulations and experiments. Journal of Biomechanical Engineering. 2005; 127(5):782–797. [PubMed: 16248308]
56. Borazjani I, Ge L, Sotiropoulos F. High-resolution fluidstructure interaction simulations of flow through a bi-leaet mechanical heart valve in an anatomic aorta. Annals of Biomedical Engineering. 2010; 38:326–344.10.1007/s10439-009-9807-x [PubMed: 19806458]

57. Gilmanov A, Sotiropoulos F. A hybrid cartesian/immersed boundary method for simulating flows with 3d, geometrically complex, moving bodies. Journal of Computational Physics. 2005; 207(2): 457.
58. Rodriguez L, Thomas J, Monterroso V, Weyman A, Harrigan P, Mueller L, Levine R. Validation of the proximal flow convergence method. Calculation of orifice area in patients with mitral stenosis. Circulation. 1993; 88(3):1157–1165. [PubMed: 8353878]
59. Henry W, Griffith J, Michaelis L, McIntosh C, Morrow A, Epstein S. Measurement of mitral orifice area in patients with mitral valve disease by real-time, two-dimensional echocardiography. Circulation. 1975; 51(5):827–831. [PubMed: 1122586]
60. Le, T.; Bukkapatnam, S.; Sangasoongsong, A.; Komanduri, R. Towards virtual instruments for cardiovascular healthcare: Real-time modeling of cardiovascular dynamics using ecg signals. Automation Science and Engineering (CASE), 2010 IEEE Conference on; 2010. p. 903-910.
61. Nash MP, Panfilov AV. Electromechanical model of excitable tissue to study reentrant cardiac arrhythmias. Progress in Biophysics and Molecular Biology. 2004; 85(2-3):501–522. modelling Cellular and Tissue Function. [PubMed: 15142759]
62. Chadwick R. Mechanics of the left ventricle. Biophysical Journal. 1982; 39(3):279–288. [PubMed: 7139027]
63. Panfilov A, Hogeweg P. Spiral breakup in a modified fitzhugh-nagumo model. Physics Letters A. 1993; 176(5):295–299.
64. Aliev RR, Panfilov AV. A simple two-variable model of cardiac excitation. Chaos, Solitons and Fractals. 1996; 7(3):293–301.
65. FitzHugh R. Impulses and physiological states in theoretical models of nerve membrane. Biophysical Journal. 1961; 1(6):445–466. [PubMed: 19431309]
66. Rogers J, McCulloch A. A collocation-galerkin finite element model of cardiac action potential propagation. Biomedical Engineering, IEEE Transactions on. 1994; 41(8):743–757.
67. Kanai H. Propagation of spontaneously actuated pulsive vibration in human heart wall and in vivo viscoelasticity estimation. Ultrasonics, Ferroelectrics and Frequency Control, IEEE Transactions on. 2005; 52(11):1931–1942.
68. Pernot M, Fujikura K, Fung-Kee-Fung SD, Konofagou EE. Ecg-gated, mechanical and electromechanical wave imaging of cardiovascular tissues in vivo. Ultrasound in Medicine and Biology. 2007; 33(7):1075–1085. [PubMed: 17507146]
69. Sengupta PP, Tondato F, Khandheria BK, Belohlavek M, Jahangir A. Electromechanical activation sequence in normal heart. Heart Failure Clinics. 2008; 4(3):303–314. [PubMed: 18598982]
70. Beyar R, Sideman S. A computer study of the left ventricular performance based on fiber structure, sarcomere dynamics, and transmural electrical propagation velocity. Circ Res. 1984; 55(3):358–375. [PubMed: 6467528]
71. Miller W, Geselowitz D. Simulation studies of the electrocardiogram. i. the normal heart. Circ Res. 1978; 43(2):301–315. [PubMed: 668061]
72. Jung B, Markl M, Foll D, Hennig J. Investigating myocardial motion by MRI using tissue phase mapping. Eur J Cardiothorac Surg. 2006; 29(Supplement 1):S150–157. [PubMed: 16563784]
73. Yoganathan AP, He Z, Casey Jones S. Fluid mechanics of heart valves. Annual Review of Biomedical Engineering. 2004; 6(1):331–362.
74. Kuttler U, Wall W. Fixed-point fluidstructure interaction solvers with dynamic relaxation. Computational Mechanics. 2008; 43:61–72.
75. Le, TB. Ph D thesis. University of Minnesota; United States: 2011. A computational framework for simulating cardiovascular flows in patient-specific anatomies.
76. Gilmanov A, Sotiropoulos F, Balaras E. A general reconstruction algorithm for simulating flows with complex 3d immersed boundaries on cartesian grids. Journal of Computational Physics. 2003; 191(2):660–669.
77. Le TB, Borazjani I, Kang S, Sotiropoulos F. On the structure of vortex rings from inclined nozzles. Journal of Fluid Mechanics. 2011; 686:1–33.
78. Webster DR, Longmire EK. Vortex rings from cylinders with inclined exits. Physics of Fluids. 1998; 10(2):400–416.

79. Troolin DR, Longmire EK. Volumetric velocity measurements of vortex rings from inclined exits. Experiments in Fluids. 2010; 48:409–420.
80. Kheradvar A, Gharib M. On mitral valve dynamics and its connection to early diastolic flow. Annals of Biomedical Engineering. 2009; 37:1–13. [PubMed: 18982451]
81. Fujimoto S, Mohiaddin RH, Parker KH, Gibson DG. Magnetic resonance velocity mapping of normal human transmitral velocity profiles. Heart and Vessels. 1995; 10:236–240. [PubMed: 8903998]
82. Port S, Cobb FR, Coleman RE, Jones RH. Effect of age on the response of the left ventricular ejection fraction to exercise. New England Journal of Medicine. 1980; 303(20):1133–1137. [PubMed: 7421930]
83. Remme EW, Lyseggen E, Helle-Valle T, Opdahl A, Pettersen E, Vartdal T, Ragnarsson A, Ljosland M, Ihlen H, Edvardsen T, Smiseth OA. Mechanisms of Preejection and Postejection Velocity Spikes in Left Ventricular Myocardium: Interaction Between Wall Deformation and Valve Events. Circulation. 2008; 118(4):373–380. [PubMed: 18606917]
84. Buckberg GD, Mahajan A, Jung B, Markl M, Hennig J, Ballester-Rodes M. Mri myocardial motion and fiber tracking: a confirmation of knowledge from different imaging modalities. Eur J Cardiothorac Surg. 2006; 29(1):165–177.
85. Gatehouse P, Keegan J, Crowe L, Masood S, Mohiaddin R, Kreitner K-F, Firmin D. Applications of phase-contrast flow and velocity imaging in cardiovascular mri. European Radiology. 2005; 15:2172–2184. [PubMed: 16003509]
86. Thomas J, AE W. Echocardiographic doppler evaluation of left ventricular diastolic function. physics and physiology. Circulation. 1991; 84:977–990. [PubMed: 1884473]
87. Oh JK, Appleton CP, Hatle LK, Nishimura RA, Seward JB, Tajik A. The noninvasive assessment of left ventricular diastolic function with two-dimensional and doppler echocardiography. Journal of the American Society of Echocardiography. 1997; 10(3):246–270. [PubMed: 9109691]
88. Kim WY, Walker PG, Pedersen EM, Poulsen JK, Oyre S, Houlind K, Yoganathan AP. Left ventricular blood flow patterns in normal subjects: A quantitative analysis by three-dimensional magnetic resonance velocity mapping. Journal of the American College of Cardiology. 1995; 26(1):224–238. [PubMed: 7797756]
89. Sabbah H, Khaja F, Brymer J, McFarland T, Albert D, Snyder J, Goldstein S, Stein P. Noninvasive evaluation of left ventricular performance based on peak aortic blood acceleration measured with a continuous-wave doppler velocity meter. Circulation. 1986; 74(2):323–329. [PubMed: 3731423]
90. Pollak SJ, McMillan SA, Knopff WD, Wharff R, Yoganathan AP, Felner JM. Cardiac evaluation of women distance runners by echocardiographic color doppler flow mapping. Journal of the American College of Cardiology. 1988; 11(1):89–93. [PubMed: 2961794]
91. Sengupta PP, Khandheria BK, Korinek J, Wang J, Belohlavek M. Biphasic tissue Doppler waveforms during isovolumic phases are associated with asynchronous deformation of subendocardial and subepicardial layers. J Appl Physiol. 2005; 99(3):1104–1111. [PubMed: 15905326]
92. Dasi LP, Simon HA, Sucosky P, Yoganathan AP. Fluid mechanics of artificial heart valves. Clinical and Experimental Pharmacology and Physiology. 2009; 36(2):225–237. [PubMed: 19220329]
93. Long Q, Merrifield R, Yang GZ, Xu XY, Kilner PJ, Firmin DN. The influence of inflow boundary conditions on intra left ventricle flow predictions. Journal of Biomechanical Engineering. 2003; 125(6):922–927. [PubMed: 14986421]
94. Takatsuji H, Mikami T, Urasawa K, Teranishi J-I, Onozuka H, Takagi C, Makita Y, Matsuo H, Kusuoka H, Kitabatake A. A new approach for evaluation of left ventricular diastolic function: Spatial and temporal analysis of left ventricular filling flow propagation by color m-mode doppler echocardiography. Journal of the American College of Cardiology. 1996; 27(2):365–371. [PubMed: 8557907]
95. Kilner PJ, Yang G-Z, Wilkes AJ, Mohiaddin RH, Firmin DN, Yacoub MH. Asymmetric redirection of flow through the heart. Nature. 404
96. Le TB, Sotiropoulos F. On the three-dimensional vortical structure of early diastolic flow in a patient-specific left ventricle. European Journal of Mechanics - B/Fluids. 2012; 35(0):20–24.

97. Hunt, J.; Wray, A.; Moin, P. Proc 1988 Summer Program. Stanford N.A.S.A. Centre for Turb Res CTR-S88; Eddies, streams, and convergence zones in turbulent flows.

98. Borazjani I, Sotiropoulos F. The effect of implantation orientation of a bileaflet mechanical heart valve on kinematics and hemodynamics in an anatomic aorta. Journal of Biomechanical Engineering. 2010; 132(11):111005. [PubMed: 21034146]

99. Grinberg L, Karniadakis G. Outflow boundary conditions for arterial networks with multiple outlets. Annals of Biomedical Engineering. 2008; 36:1496–1514. [PubMed: 18612828]

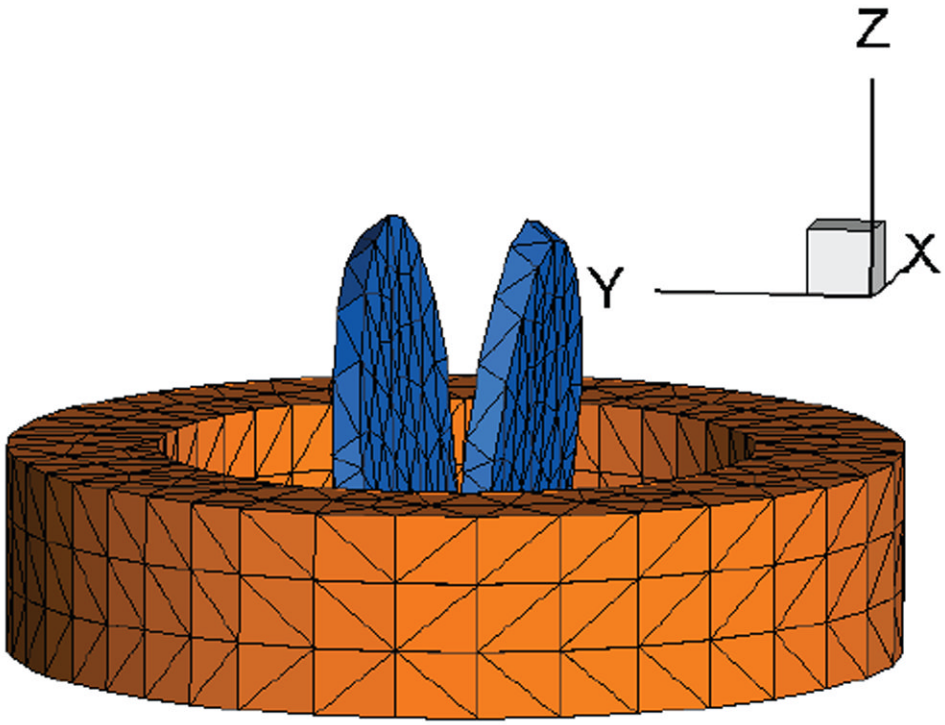

Figure 1.
A bi-leaflet mechanical heart valve is placed at the aortic position with anatomic orientation. The symmetric plane of the BMHV ($x = 0$) goes through the left ventricular apex. The implantation is shown in Fig. 5.

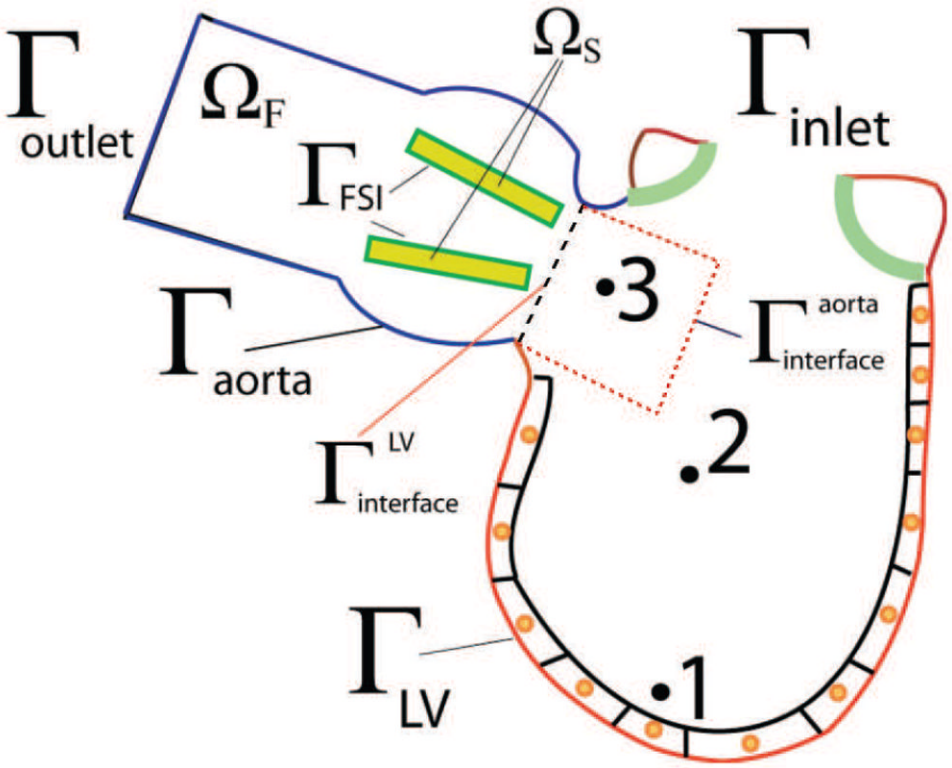

Figure 2.

The sketch depicts the computational framework and the partition between the fluid and the solid domains. Γ_{inlet} and Γ_{outlet} are the inlet and outlet of the computational domain. Γ_{aorta} is the aortic portion of the domain where the no-slip boundary condition is applied. Γ_{FSI} is the interface between leaflets Ω_s and the blood flow Ω_f, which is simulated via the fluid-structure interaction methodology. The Γ_{LV} represents the endocardium surface where the left ventricle beats. The kinematics of Γ_{LV} is simulated by the cell-based model as discussed in section 2.1.

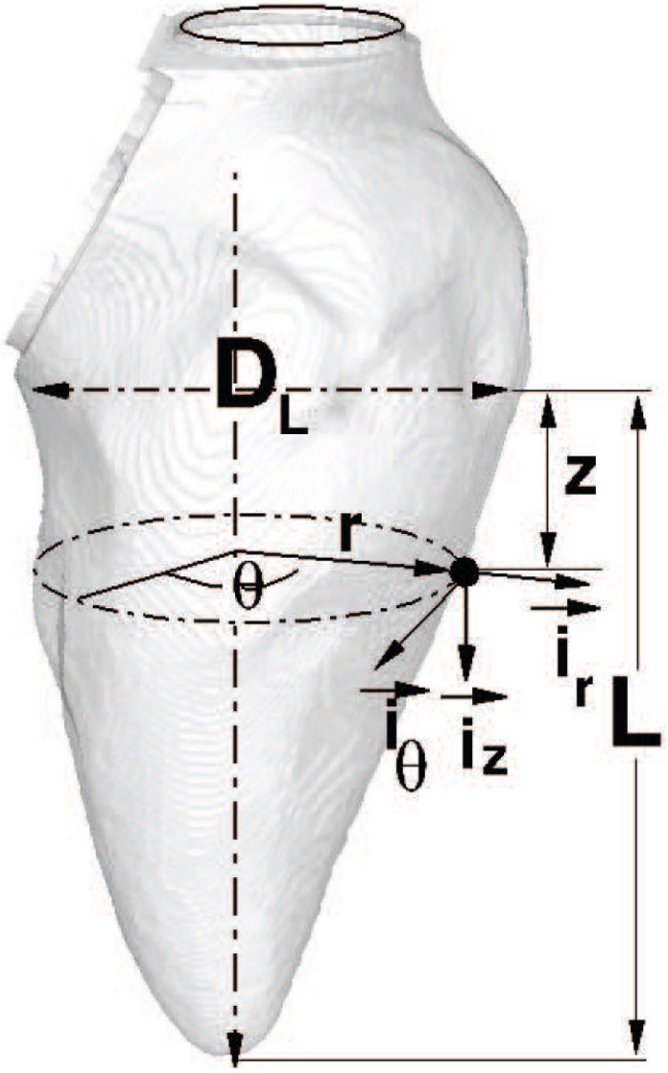

Figure 3.

The left ventricle model reconstructed from MRI images includes the left ventricle outflow tract (LVOT) and the left ventricular chamber. (r, θ, z) is the cylindrical coordinate system defined for the LV with corresponding unit vectors $\mathbf{i}_r$, $\mathbf{i}_\theta$, and $\mathbf{i}_z$. L and D_L are the lengths of the long and short LV axes, respectively.

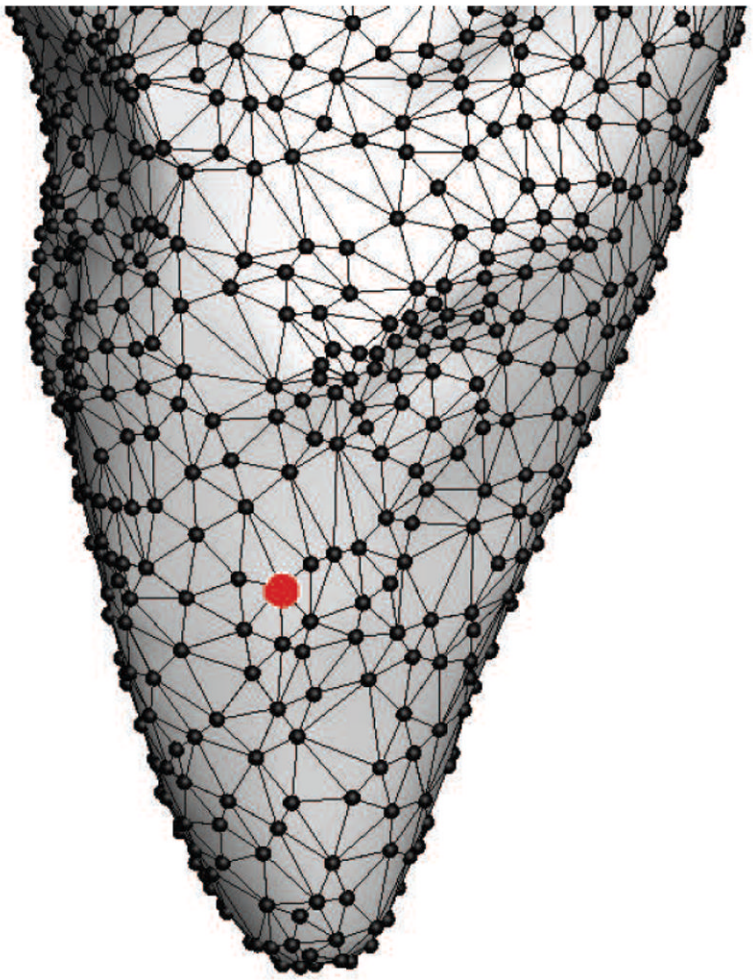

Figure 4.
The moving LV model, discretized with the unstructured grid is immersed in a background stationary curvilinear mesh as required by the CURVIB method (see Fig. 5). The blood flow is driven by the LV wall motion resulting from the cell-activation model in section 2.1. The "red" material point denotes one material point on the LV surface.

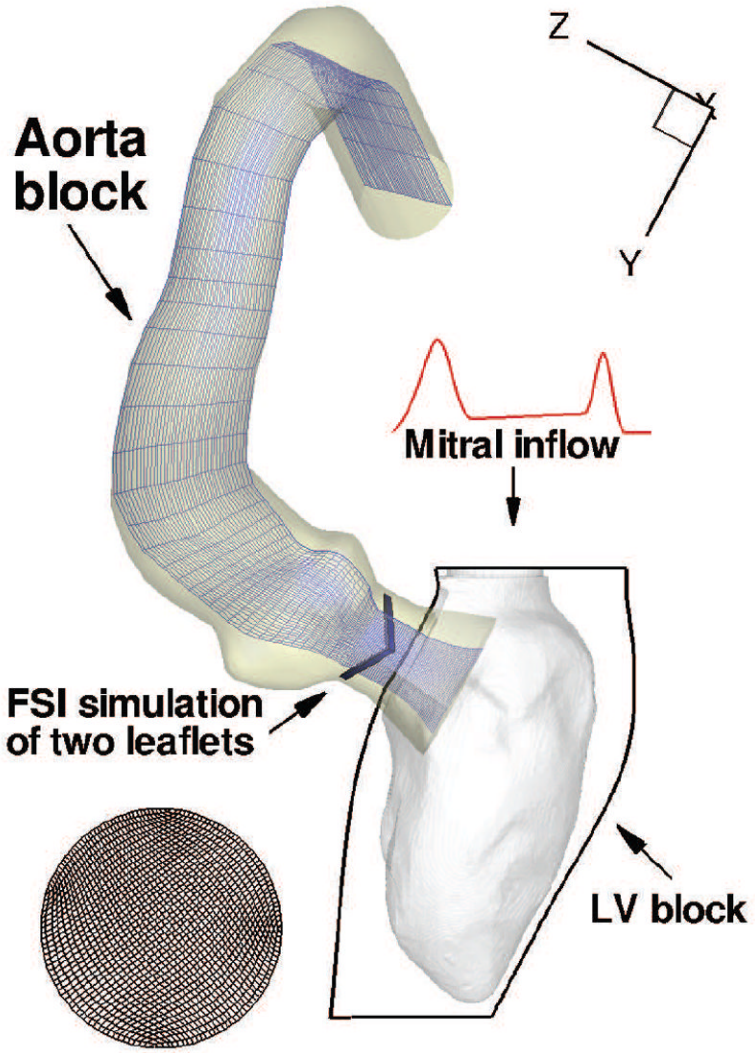

Figure 5.

a)The computational grid consists of two distinct blocks: the left ventricle block and the aorta block. The left ventricular block is a structured grid of size 161 × 281 × 161. For clarity, the 3D background grid is shown only on the symmetry plane ($x = 0$) of the BMHV for every four grid line. The aorta block is a body fitted mesh of size 161 × 161 × 401. For clarity, every one out of four grid points is shown. At the mitral position, uniform pulsatile flow $Q_m(t)$ is specified as boundary condition and the mitral valve is assumed to be fully open during diastole.

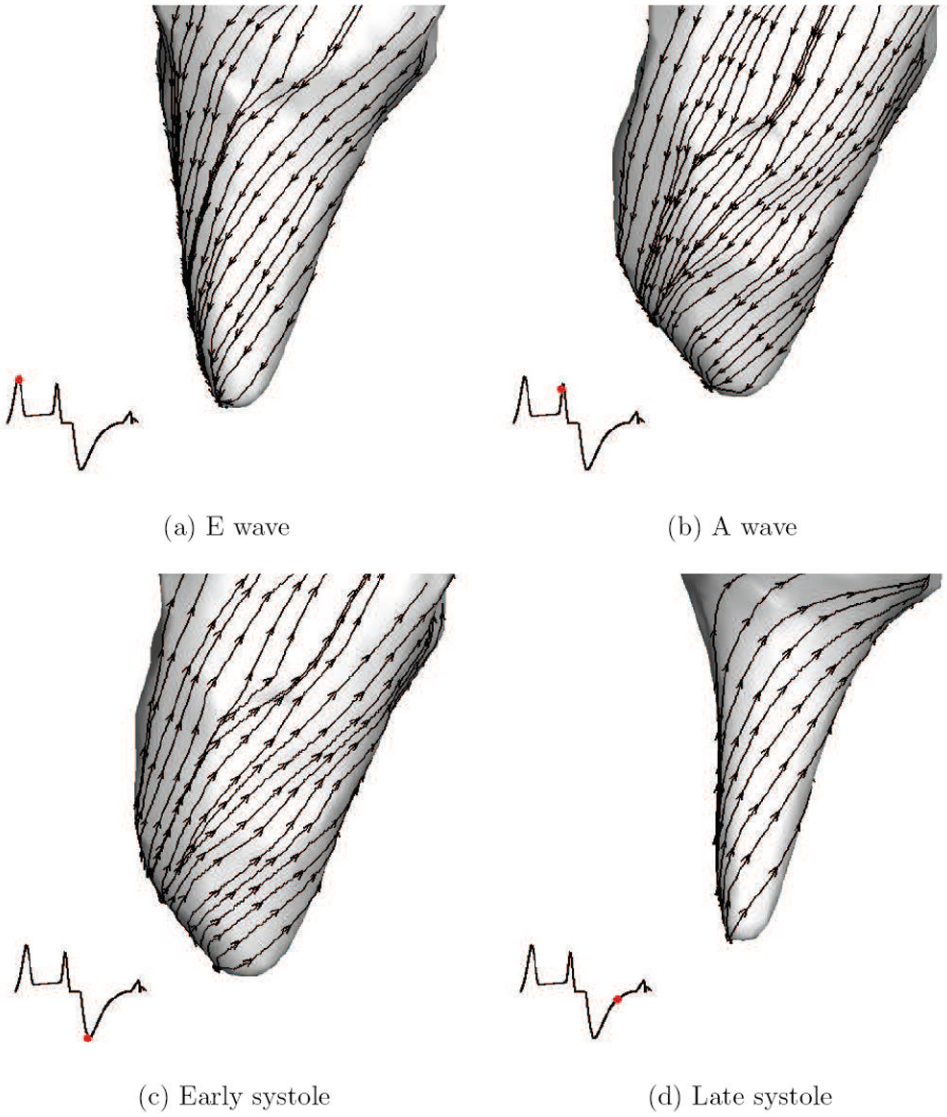

Figure 6.
The deformation of the endocardium surface during one cardiac cycle from diastole to systole. The instantaneous wall velocity field is indicated by the projected streamlines on the endocardium surface. The red dot in the inset shows the time instance in the cardiac cycle.

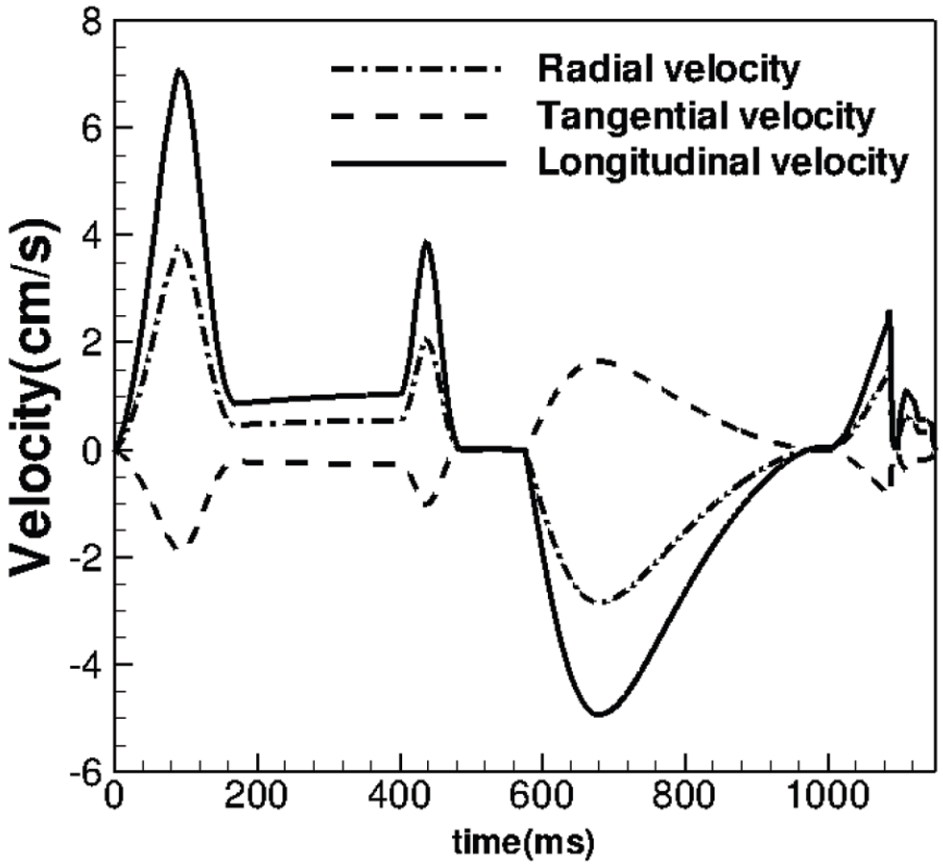

Figure 7.
Calculated time series of the three velocity components for the material point shown in Fig. 4. For the definition of radial (v^r), tangential (v^θ) and longitudinal (v^z) velocity components, see Eqs. 2 to 12 and the parameters in Table 1.

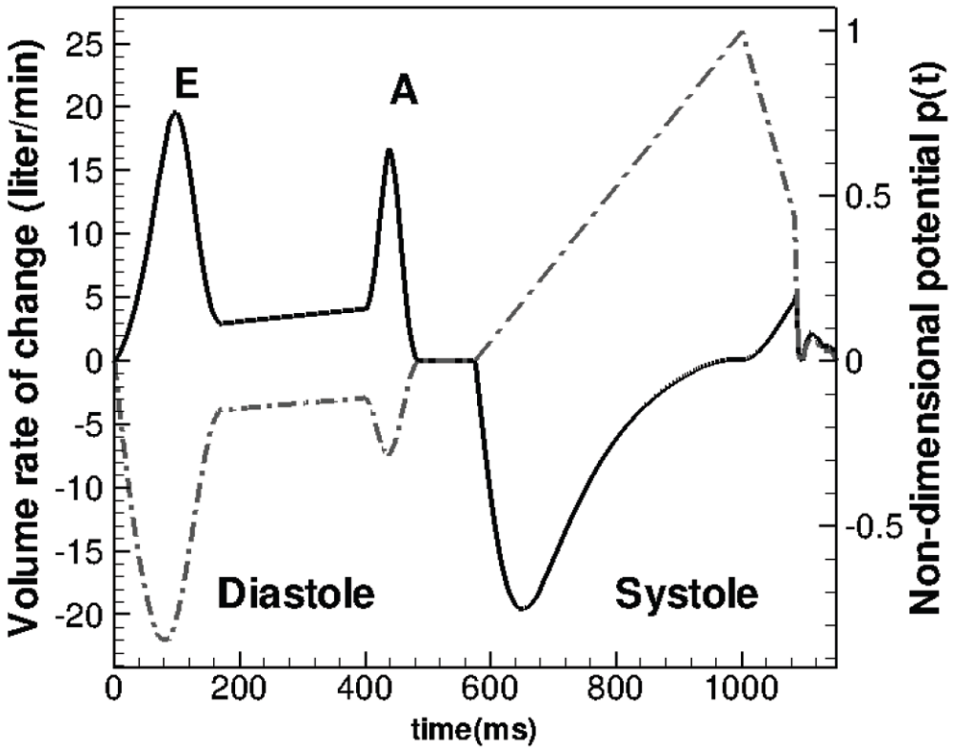

Figure 8.
The left ventricle volume rate of change during one cardiac cycle. There are two distinct positive E-wave and A-wave peaks separated by the diastasis during diastole. The negative peak is the systolic peak.

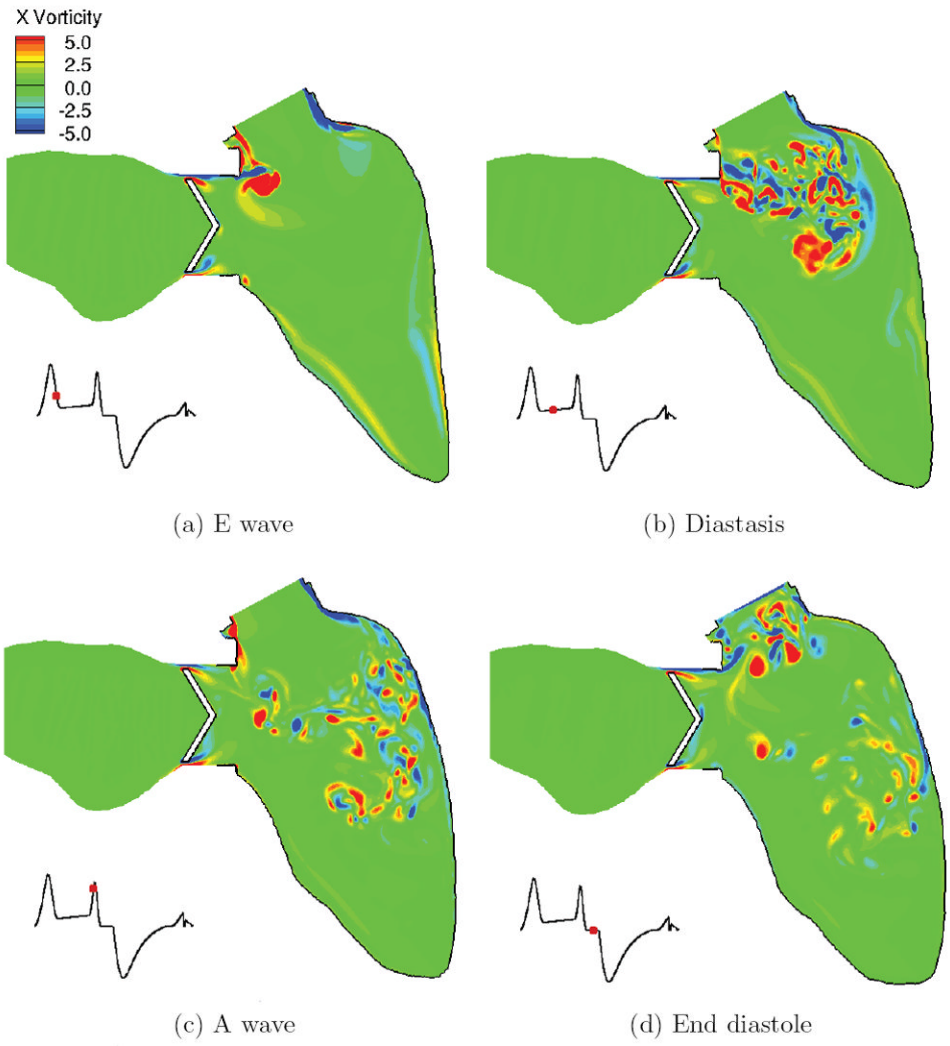

Figure 9.

The formation and breakup of mitral vortex rings during diastole: a) the formation of mitral vortex ring after the E-wave; b) The breakup of the mitral vortex ring in to small scales; c) the evolution of the intraventricular flow during diastasis; d) The flow at the end of diastole. The flow is visualized using the out-of-plane vorticity ω_x on the symmetry plane of the BMHV ($x = 0$). The red dot in the inset shows the time instance in the cardiac cycle. The upper and lower leaflet are denoted as leaflet 1 and 2, respectively.

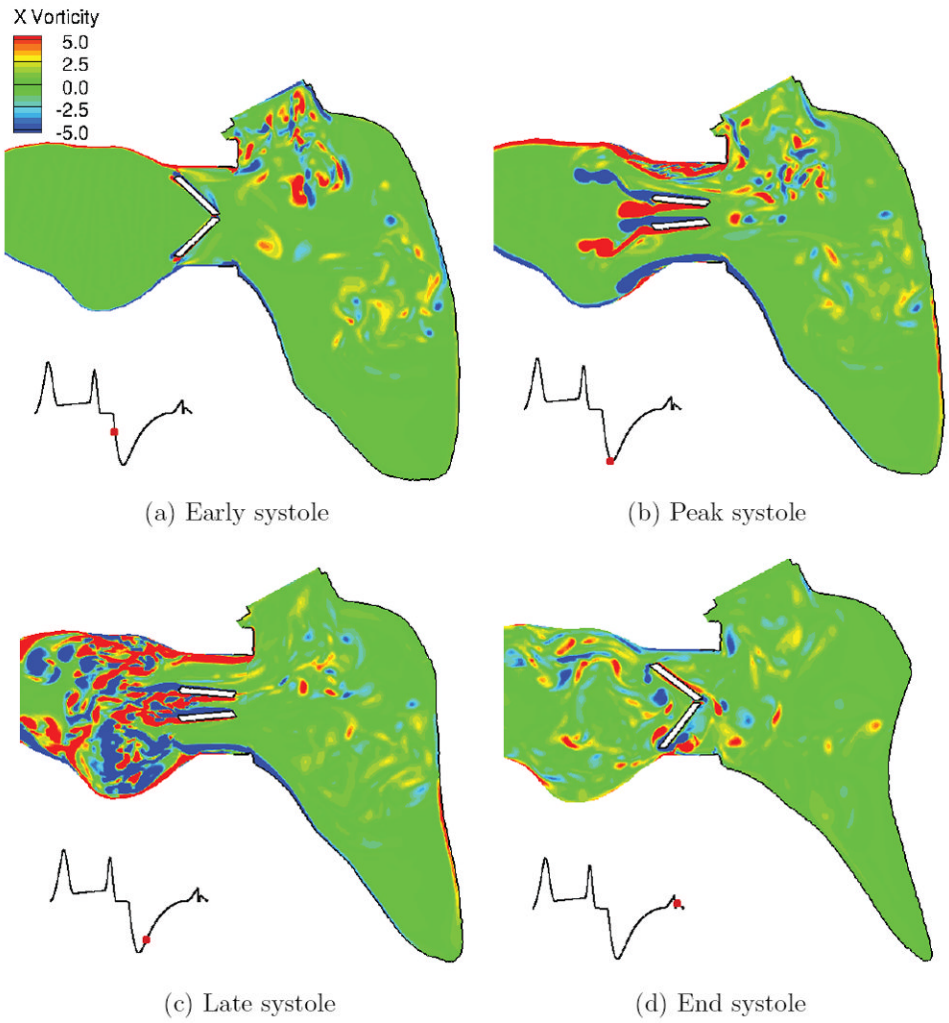

Figure 10.

The ejection of blood flow from the left ventricle into the aorta visualized by the out-of-plane vorticity ω_x on the symmetry plane of the BMHV ($x = 0$): a) The existence of coherent structures inside the left ventricular chamber at the beginning of systole; b) The BMHV opens at the peak systole and induces the unstable shear layer to form on the leaflet surfaces; c) The formation of three dimensional worm-like structures inside the aortic root; d)As the BMHV closes, the leaflet 2 (lower) accelerates faster than the leaflet 1 (upper). The closure of the BMHV induces leakage flow back into the LV chamber. The red dot in the inset shows the time instance in the cardiac cycle.

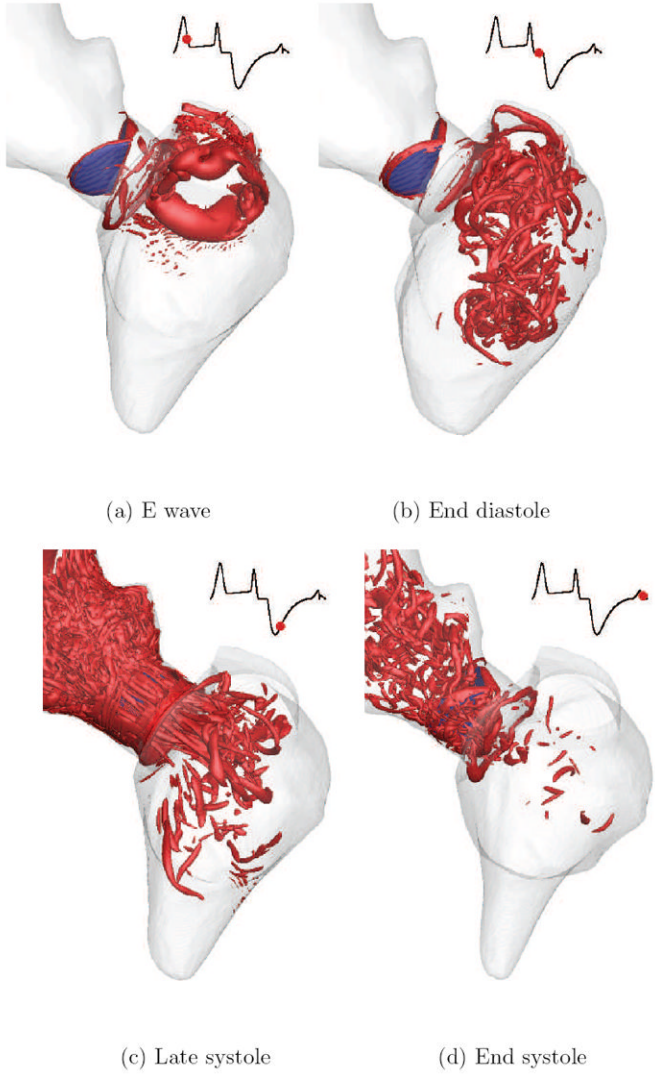

Figure 11.
The formation of coherent structures inside the left ventricular chamber during diastole in (a) and (b). The small scale structures are advected into the aorta during systole in (c) and (d). The flow is visualized by Q-criteria [97]. The view is from the apex. The red dot in the inset shows the time instance in the cardiac cycle.

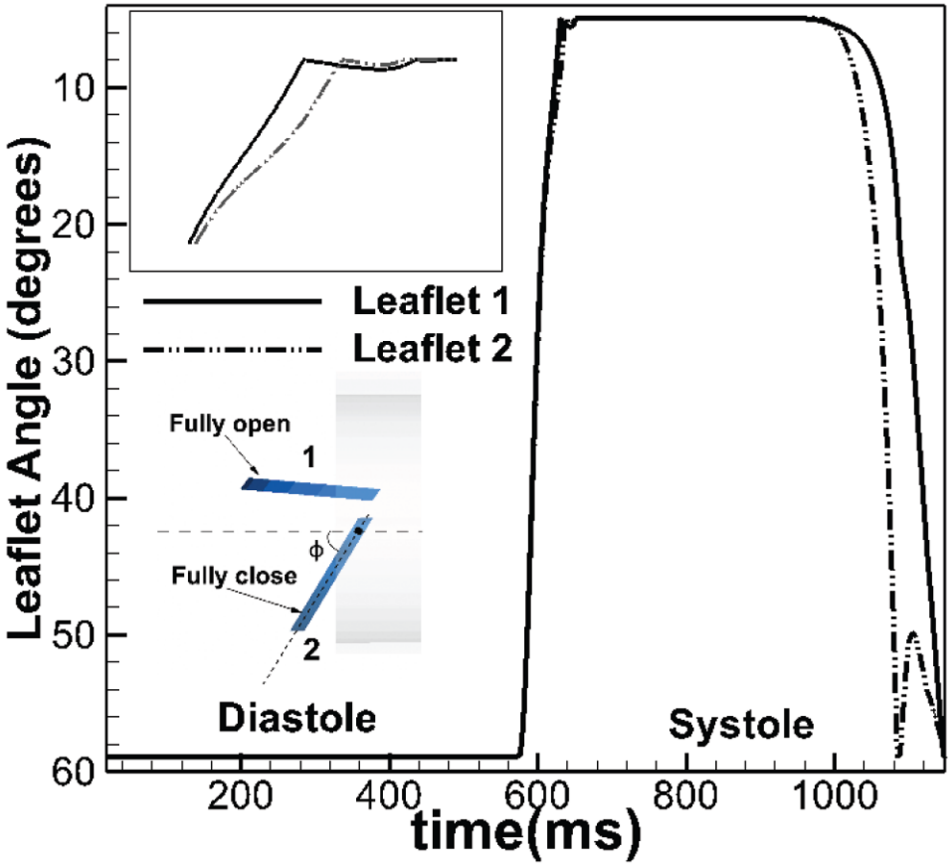

Figure 12.

The kinematic (angle ϕ) of upper leaflet (1) and lower leaflet (2) over the whole cardiac cycle. The difference of two leaflet motion is most significant near the closing phase of the BMHV. The inset shows the definition of the opening angle ϕ with fully open and fully close position.

Table 1

The non-dimensional parameters used in the left ventricular kinematic model.

Name	Systole	Diastole
c_0	1	1
c_1	0.21	0.175
c_2	0.011	0.011
c_3	0.55	0.55
t_s/T	0.87	0
f_s	0.35	0.3
κ_0	3.9	0.36
κ_1	-0.2	0
φ	-0.052	0.424
α	0.52	0.52
β	0.3	0.3
γ	0.8	0.8

Note that the left ventricular geometry is non-dimensionalized using the characteristic length scale $D_0 = 29mm$. c_0, c_1, c_2, c_3 are variables of the FitzHugh-Nagumo model. t_s is the starting time of T-wave and T is the cardiac cycle. f is the frequency of the propagating wave front. κ_0, κ_1 are the scaling factors. α, β, γ are the distributing factors of the velocity vector along radial, tangential and axial directions, respectively (see Eq. 12 for definition).

Table 2

The global parameters of the left ventricle kinematics resulting from the proposed cell-activation based model.

Parameters	Value	Definition
End systolic volume (ESV)	65 ml	Minimum of LV volume
End diastolic volume(EDV)	118 ml	Maximum of LV volume
Stroke volume (SV)	53 ml	EDV - ESV
Ejection fraction (EF)	45%	SV/EDV
Peak E-wave velocity	0.7 m/s	Maximum bulk velocity at mitral orifice

All quantities are well within the physiologic range.